nature research

https://doi.org/10.1038/s41561-020-00646-4

Supplementary information

Permian–Triassic mass extinction pulses driven by major marine carbon cycle perturbations

In the format provided by the authors and unedited

Supplementary Information to

'*Permian-Triassic mass extinction pulses driven by major marine carbon cycle perturbations*'

by Jurikova, H., Gutjahr, M., Wallmann, K., Flögel, S., Liebetrau, V., Posenato, R., Angiolini, L., Garbelli, C., Brand, U., Wiedenbeck, M. & Eisenhauer, A.

Contents:

S1. Stratigraphy and duration of the Permian-Triassic extinction in the Southern Alps

The Upper Permian succession of the eastern Southern Alps – Dolomites and Venetian Prealps – shows an overall transgressive trend, punctuated by some transgressive-regressive cycles. The succession, up to 1000 m thick in the depocentre, is represented by the Val Gardena Sandstone red beds topped and interfingered by evaporites and shallow marine carbonates of the Bellerophon Formation. East of Adige Valley, the Bellerophon Formation is overlain by the oolitic and microbial limestone of the Tesero Member of the Werfen Formation, where the Permian-Triassic boundary (PTB) has been located at about 1.3 m above the formational base in the parastratotype Bulla section (Perri & Farabegoli, 2003).

The Lopingian succession of the Bellerophon Formation yields rich and abundant marine

fossil assemblages, which have been studied by geologists since the 19th century (see Posenato, 2010 for an overview). The appearance of *Comelicania* in the Dolomites occurs in the Bellerophon Fm, about 50 m below the Bellerophon-Werfen Formation boundary (BWFB), and represents the oldest samples of our record. The lower *Comelicania* beds have been correlated to the *Clarkina changxingensis* Zone of South China (Posenato, 2010; Farabegoli et al., 2007), which has a duration of about 1.063 Ma (Yuan et al., 2014). The later biozones, before the onset of the mass extinction, are overlain by the *C. yini* Zone, which has a calculated duration of 104 ka (Yuan et al., 2014). Therefore, the lower *Comelicania* beds were deposited before the BWFB spanning a long-time interval ranging from 1167 to 104 ka. An exact age of these samples is difficult to calculate, however, it cannot be younger than preceding the carbon isotope excursion (CIE) by at least 120 ka, the age used in our record. Nevertheless, because the stable isotope composition of these specimens is within the range of samples from upper beds located before the mass extinction horizon, variations in the absolute age of these samples would not affect our reconstruction.

The uppermost 0.4−1.40 m of the Bellerophon Fm comprises the Bulla Member, composed predominantly of a dark grey fossiliferous limestone, which is referred to as the latest Changhsingian *Hindeodus praeparvus* Zone (Perri & Farabegoli, 2003; Farabegoli et al., 2007). Here, foraminifera and brachiopod diversity reaches its maximum, with the latter represented by *Comelicania*, *Comelicothyris*, *Janiceps*, *Ombonia*, *Orthothetina*, and *Septospirigella* spp. in the upper beds and *Comelicania* dominating the underlying beds (Posenato, 2010; Broglio Loriga et al., 1988; Posenato, 2001; Posenato, 2009). On the basis of biostratigraphy and depositional characteristics, the top of the Bulla Member is correlated with Bed 24e at Meishan (Posenato, 2010; Yin et al., 2001; Horacek et al., 2010; Brand et al., 2012; Fig. S1.1), which suggests a duration of approximately 10 ka (Burgess et al., 2014; Shen et al., 2011).

The skeletal limestone of the Bulla Formation is separated from the overlaying ooid grainstone of the Tesero Member (Werfen Formation) at the BWFB by an erosional surface with a very low topographic relief (few cm at the outcrop scale). The wide geographical extension of the facies successions of Bulla Member (not affected by significant erosive truncation), the lack of karst cement and the bio-chronostratigraphic setting of the units located across the formational boundary (both belonging to the *H. preparvus* Zone) suggest a short duration for the BWFB hiatus (centennial to millennial) probably produced by a rapid

sea level drop, emersion and subsequent erosion (Farabegoli et al., 2007). The hiatus spans the top of Bed 24e and the lower part of Bed 25 which bears the sharp negative carbonate carbon isotopic anomaly ($\delta^{13}C_{carb}$) at Meishan ($\delta^{13}C_{carb}$ drops off rapidly from approximately 2 to −4 ‰ in the upper 6 cm of the 10 cm thick Bed 24e; Shen et al., 2011; Cao et al., 2009; Cao et al., 2010; Shen & Bowring, 2014), which explains the more moderate $\delta^{13}C_{carb}$ trend in the Dolomites sections (Korte & Kozur, 2005; Groves et al., 2007; Kearsey et al., 2009; Korte & Kozur, 2010; Baresel et al., 2017).We assume a duration of the hiatus of approximately 2 ka, which is reasonable considering the previously mentioned geological and biostratigraphic features of the boundary and the duration of the sharp $\delta^{13}C_{carb}$ excursion (Burgess et al., 2014).

The basal Tesero Member (5−10 cm) is composed of ooid grainstone with abundant reworked and non-reworked micro- and macrofossils. The grainstone of the above bed (app. 15 cm) yields small oomold ooids and is characterised by abundant not reworked *Ombonia* and *Orthothetina,* and rare *Janiceps* shells (Neri & Posenato, 1999; Posenato, 2001; Farabegoli et al., 2007). A dramatic decrease of foraminifer species richness and abundance, and disappearance of large brachiopods within the lower 10−20 cm of Tesero Member indicate the onset and peak of the end Permian extinction in the Dolomites (Broglio Loriga et al., 1988; Farabegoli et al., 2007; Posenato, 2009; Posenato, 2010). Accordingly, the basal Tesero Mb *Ombonia* and *Orthothetina* beds can be correlated to the top of bed Bed 25–base of Bed 26 of Meishan (Jin et al., 2000; Yin et al., 2001; Shen et al., 2011). In comparison to the Dolomites, the Meishan section is, however, very condensed. The so-called 'mass extinction interval' of Meishan, located between Bed 25 (*C. meishanensis* Zone formerly *H. praeparvus* Zone of Jiang et al., 2007) and Bed 28 (*Is. staeschei* Zone) is about 35 cm thick, with an estimated duration of about 61 ka (± 48; Burgess et al., 2014). The corresponding stratigraphic interval at Tesero section is about 25 m thick.

The subsequent beds (Mixed fauna beds; Neri & Pasini, 1985; Posenato, 2009) are characterised by the appearance of microbialites and '*Crurithyris*' fauna, yielding small and rare cosmopolitan brachiopods (Broglio Loriga et al., 1988; Chen et al., 2006l Posenato, 2009). The last rhynchonelliform brachiopods are common only in the Tesero section represented by *Orbicoelia* and *Teserina*. The youngest analysed specimens were located at 2.4 m (bed CNT10, *Orbicoelia*) and 2.6 m (bed CNT11A, *Teserina*) above the BWFB (Posenato, 2011).

The index fossil *Hindeodus changxingensis* occurs at 1.30 m of the Tesero section and marks the last Permian conodont zone in South China with first appearance in Bed 26 (Jiang et al., 2007; Metcalfe et al., 2007). In the Dolomites Bulla section, the FO of *Hindeodus parvus,* marker of the PTB, occurs at 1.30 m above the BWFB, while in the Tesero section, it enters later, as soon as conodonts recur at the top of the conodont-barren interval (Perri & Farabegoli, 2003). Following a previous study (Perri & Farabegoli, 2003), based on available conodont data we locate the PTB in the Tesero section close to the entry of *H. changxingensis*, which suggests that the most probable first occurrence of *H. parvus* slightly predates bed CNT11A (or TS10A; Perri & Farabegoli, 2003). This locates the *Teserina* bed within the lowermost *H. parvus* zone, implying an Early Triassic age, therefore, it can be correlated to the Bed 27c of Meishan.

Based on our correlation, the Dolomites' PTB section can be aligned to Meishan for which absolute ages are available. Using the geochronology and sediment accumulation rates for Meishan (Burgess et al., 2014) the timing of changes in the geochemical record can be constrained (Table S1.1). Accordingly, the duration between the CIE and the PTB is about 50 ka (highly comparable and within the uncertainties of the 61 ka established for Meishan, based on the difference between the bracketing dated ash beds; Burgess et al., 2014).

Section	**Stratigraphic location**	**Sedimentary rates (cm/ka)**	**Source**
Meishan GSSP	Bed 22-25	2.6	*Burgess et al. (2014)*
	Bed 25-28	0.36	
	Bed 28-29	0.58	
Southern Alps	Upper Bellerophon Fm.	20	*Estimated (this study)*
	Bulla Mb.	25	
	Tesero Mb.	100	

Table S1.1. Sedimentation rates for Meishan (from Burgess et al., 2014) and the estimated rates for Southern Alps (Dolomites) based on our correlation of Dolomites to Meishan.

Our proposed correlation between the Dolomite successions and Meishan GSSP is outlined in Figure S1.1 below. For the purpose of presenting a concise picture of the aligned sections and straightforward comparison to the geochronological data (Burgess et al., 2014) this figure principally illustrates the different $\delta^{13}C_{carb}$ trends. We note, however, that a direct comparison merely based on $\delta^{13}C_{carb}$ trend would not be fully representative, and as discussed above, biostratigraphic features and extinction patterns have to be considered for a proper correlation.

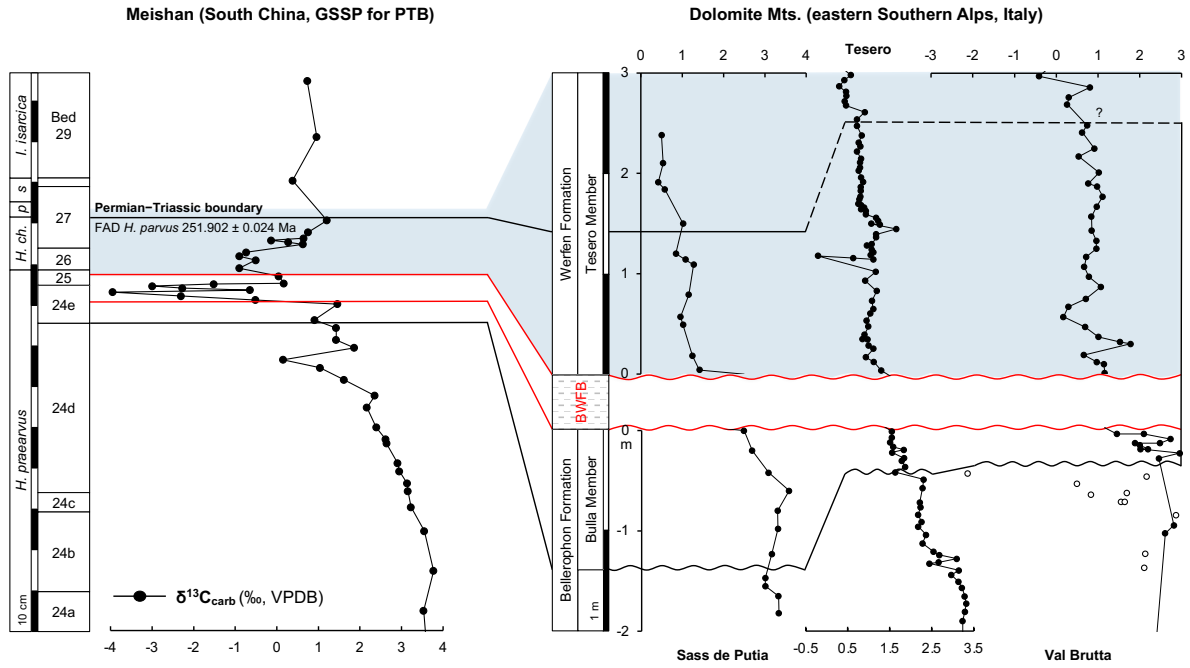

Figure S1.1. Comparative correlation of stratigraphy and carbonate carbon isotopic composition ($\delta^{13}C_{carb}$) trends between Meishan GSSP (Cao et al., 2009) and the three studied Dolomites successions: Sass de Putia (Korte & Kozur, 2005), Tesero (Groves et al., 2007) and Val Brutta (Kearsey et al., 2009). Open symbols for Val Brutta represent recrystallized material and were excluded. Conodont zones (chronologically): *Hindeodus praeparvus, H. changxingensis, H. parvus* (about 22 m thick included in *Is. lobata* Zone at the Tesero section), *Isarcicella staeschei* (about 2 m thick at the Tesero section), and *Isarcicella isarcica* (FO at about 24 m above BWFB at the Tesero section; conodont data are from Perri & Farabegoli 2003; Farabegoli & Perri, 2012); conodont zones in China are according to Jiang et al. (2007). Ages and geochronology are from Burgess et al. (2014).

References

Perri, M.C. & Farabegoli, E. Conodonts across the Permian-Triassic boundary in the Southern Alps. *Courier Forschungsinstitut Senckenberg* **245**, 281–313 (2003).

Posenato, R. Marine biotic events in the Lopingian succession and latest Permian extinction in the Southern Alps (Italy). *Geol. J.* **45**, 195−215 (2010).

Farabegoli, E., Perri, M.C. & Posenato, R. Environmental and biotic changes across the Permian–Triassic boundary in western Tethys: the Bulla parastratotype, Italy. *Glob. Planet. Change* **55**, 109–135 (2007).

Yuan, D.-X. *et al.* Revised conodont-based integrated high-resolution timescale for the Changhsingian Stage and end-Permian extinction interval at the Meishan sections, South China. *Lithos* **204**, 220-245 (2014).

Broglio Loriga, C., Neri, C., Pasini, M. & Posenato, R. Marine fossil assemblages from Upper Permian to lowermost Triassic in the western Dolomites (Italy). In: Cassinis G. (Ed.) *Permian and Permian–Triassic boundary in the South-Alpine segment of the western Tethys, and additional reports.* Memorie della Societa Geologica Italiana 34, 5–44

(1988).

Posenato, R. The athyridoids of the transitional beds between Bellerophon and Werfen formations (uppermost Permian, Southern Alps, Italy). *Riv. Ital. Paleontol S.* ***1071***, 197–226 (2001).

Posenato, R. Survival patterns of macrobenthic marine assemblages during the end-Permian mass extinction in the western Tethys (Dolomites, Italy). *Palaeogeogr. Palaeoclimatol. Palaeoecol.* **280**, 150–167 (2009).

Yin, H., Zhang, K., Tong, J., Yang, Z. & Wu, S. The global stratotype section and point (GSSP) of the Permian-Triassic boundary. *Episodes* **24**, 102–114 (2001).

Horacek, M., Povoden, E., Richoz, S. & Brandner, R. High-resolution carbon isotope changes, litho- and magnetostratigraphy across Permian-Triassic Boundary section in the Dolomites, N-Italy. New constraints for global correlation. *Palaeogeogr. Palaeoclimatol. Palaeoecol.* **290**, 58–64 (2010).

Brand, U. *et al.* The end-Permian mass extinction: A rapid volcanic CO_2 and CH_4-climatic catastrophe. *Chem. Geol.* **323**, 121−144 (2012).

Burgess, S.D., Bowring, S. & Shen, S.-Z. High-precision timeline for Earth's most severe extinction. *Proc. Natl. Acad. Sci. U.S.A.* **111**, 3316–3321 (2014).

Shen, S.-Z. *et al.* Calibrating the End-Permian Mass Extinction. *Science* **334**, 1367–1372 (2011).

Cao, C.Q. *et al.* Biogeochemical evidence for euxinic oceans and ecological disturbance presaging the end-Permian mass extinction event. *Earth Planet. Sci. Lett.* **281**, 188–201 (2009).

Cao, C.Q. *et al.* Pattern of $\delta^{13}C_{carb}$ and implication for geological events during the Permian-Triassic transition is South China. *Geol. J.* ***45***, 186–194 (2010).

Shen, S.-Z. & Bowring, S.A. The end-Permian mass extinction: a still unexplained catastrophe. *Natl Sci. Rev.* **1**, 492–495 (2014).

Korte, C. & Kozur, H.W. Carbon isotope stratigraphy across the Permian/Triassic boundary at Jolfa (NW-Iran), Peitlerkofel (Sas de Pütia, Sass de Putia), Pufels (Bula, Bulla), Tesero (all three Southern Alps, Italy) and Gerennavár (Bükk Mts., Hungary). *J. Alpine Geol.* **47**, 119–135 (2005).

Groves, J.R., Rettori, R., Payne J.L., Boyce, M.D. & Altiner, D. End-Permian mass extinction of lagenide foraminifers in the southern Alps (northern Italy). *J. Paleont.* **8**, 415–434 (2007).

Kearsey, T., Twichett, R.J., Price, G.D. & Grimes, S.T. Isotope excursion and palaeotemperature estimates from the Permian/Triassic boundary in the Southern Alps (Italy). *Palaeogeogr. Palaeoclimatol. Palaeoecol.* **279**, 29–40 (2009).

Korte, C. & Kozur, H.W. Carbon-isotope stratigraphy across the Permian-Triassic boundary: A review. *J. Asian Earth Sci.* **39**, 215–235 (2010).

Baresel, B. *et al.* Timing of global regression and microbial bloom linked with the Permian-Triassic boundary mass extinction: implications for driving mechanisms. *Sci. Rep.* **7**, 43630 (2017).

Neri, C. & Posenato, R. Sedimentary and bio-chronostratigraphical aspects of the P/T boundary in the eastern Southern Alps. In: Cassinis G. (Ed.) *Stratigraphy and facies of the Permian deposits between eastern Lombardy and the western Dolomites*. Field Trip

Guidebook 23–25 September 1999, Pavia 35–42 (1999).

Jin, Y.G. *et al.* Pattern of Marine Mass Extinction Near the Permian-Triassic Boundary in South China. *Science* **289**, 432–436 (2000).

Jiang, H. *et al.* Restudy of conodont zonation and evolution across the P/T boundary at Meishan section, Changxing, Zhejiang, China. *Glob. Planet. Change* **55**, 39–55 (2007)

Neri, C. & Pasini, M. A mixed fauna at the Permian-Triassic boundary, Tesero section, western Dolomites (Italy). *Bollettino della Società Paleontologica Italiana* **23**, 113–117 (1985).

Chen, Z.-Q., Kaiho, K., George, A.D. & Tong J. Survival brachiopod faunas of the end-Permian mass extinction from the Southern Alps (Italy) and South China. *Geological Magazine* **143**, 301–327 (2006).

Posenato, R. Latest Changhsingian orthotetid brachiopods in the Dolomites (Southern Alps, Italy): ecological opportunists at the peak of the end-Permian mass extinction. *J. Paleontol.* **85**, 58–68 (2011).

Metcalfe, I., Nicoll, R.S. & Wardlaw, B.R. Conodont index fossil *Hindeodus changxingensis* Wang fingers greatest mass extinction event. *Palaeoworld* **16**, 202–207 (2007).

Farabegoli, E. & Perri, M.C. Millennial physical events and the end-Permian mass mortality in the western Palaeotethys: Timing and primary causes. In: Talent J.A. (Ed.) *Earth and Life. Global Biodiversity, Extinction Intervals and Biogeographic Perturbations Through Time*. Springer, 719–758 (2012).

S2. Brachiopod sample selection

A detailed list of specimens is available in the accompanying Supplementary Data file. Our record is predominantly based on well-studied brachiopods of the Class Rhynchonellata and Strophomenata originating from sections spanning the Permian-Triassic boundary (PTB; Sass de Putia, Tesero, Val Brutta) in northern Italy described in Brand et al. (2012). These samples were complemented by few additional specimens from the same sections coming from the personal collection of Renato Posenato and Lucia Angiolini. Furthermore, for a geographic comparison, few specimens of the Class Rhynchonellata (*Paracrurithyris* sp.) spanning the extinction interval from South China (Shangsi section) were also included from the study of Garbelli et al. (2017a).

Brachiopods belonging to the classes Rhynchonellata and Strophomenata dominated the late Palaeozoic seas. The shell succession of fossil Rhynchonellata is similar to the extant ones, composed of a thin outer primary layer of a granular microstructure, a secondary layer of discrete calcite fibres (the optimal target for geochemical analyses), and, sometimes, a tertiary

layer of columnar prisms (Fig. S2.1). Strophomenata became extinct during the PTB crisis and lack extant representatives. Their shell succession is similar to that of Rhynchonellata, but with a different secondary layer build of cross-bladed calcite laminae (Fig. S2.1; for further details on shell structure of the two classes see Garbelli et al., 2014 and references therein). The differences in the fabric of the secondary layer appear to be related to the mechanisms of shell secretion and the content of organic matter available to safeguard the structural units, and seem to explain the extinction of one but survival of the other (e.g. Garbelli et al., 2017a; Ye et al., 2019).

Although our $\delta^{11}B$ record combines both classes, and thus the different fabrics, the same pre-event as well as acidification conditions can be reconstructed solely based on Rhynchonellata (Fig. 1 in the manuscript). Moreover, the good agreement in $\delta^{11}B$ values of different species of Rhynchonellata and Strophomenata overlapping in one bed (wPK11B), suggests that there are no fabric-specific effects on $\delta^{11}B$ among the two classes. Considering that taxon-specific influences on $\delta^{11}B$ across marine calcifiers are typically caused by vital effects linked to the capacity of an organism to physiologically regulate its internal pH at calcification site, our data further corroborate the hypothesis that differences in metabolic cost of shell secretion, rather than substantial differences in physiological pH-buffering were decisive for the survival of a specific class over the PTB mass extinction (Garbelli et al., 2017a; Garbelli et al., 2017b).

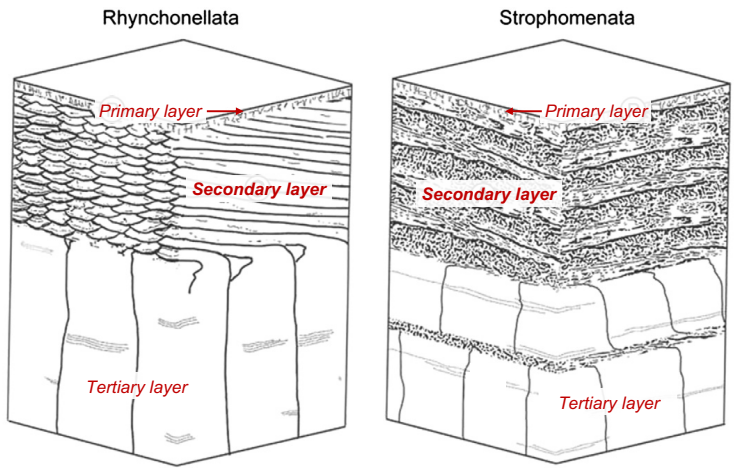

Figure S2.1. Schematic diagram of shell microstructure in three-layered brachiopods of the Class Strophomenata and Class Rhynchonellata from Garbelli et al. (2014). Primary layer forms the outermost surface and is rarely preserved in fossil shells. We measured the secondary layer, which is deemed the most suitable for geochemical analyses and present in all species.

In addition to the geochemical data shown in Extended Data Figure 1 in the main text, the good preservation of the distinct fabrics that form the secondary layer, even in the scarce specimens spanning the extinction interval (and according to our age model of earliest Triassic age), can be seen from scanning electron microscope imaging (Fig. S2.2). The shell

microstructure in both *Paracrurithyris* sp. (Rhynchonellata) and *Teserina* sp. (Strophomenata) shows clearly visible calcite fibres and cross-bladed laminae, demonstrating that the original shell structure remained intact and was not overprinted by diagenetic alterations.

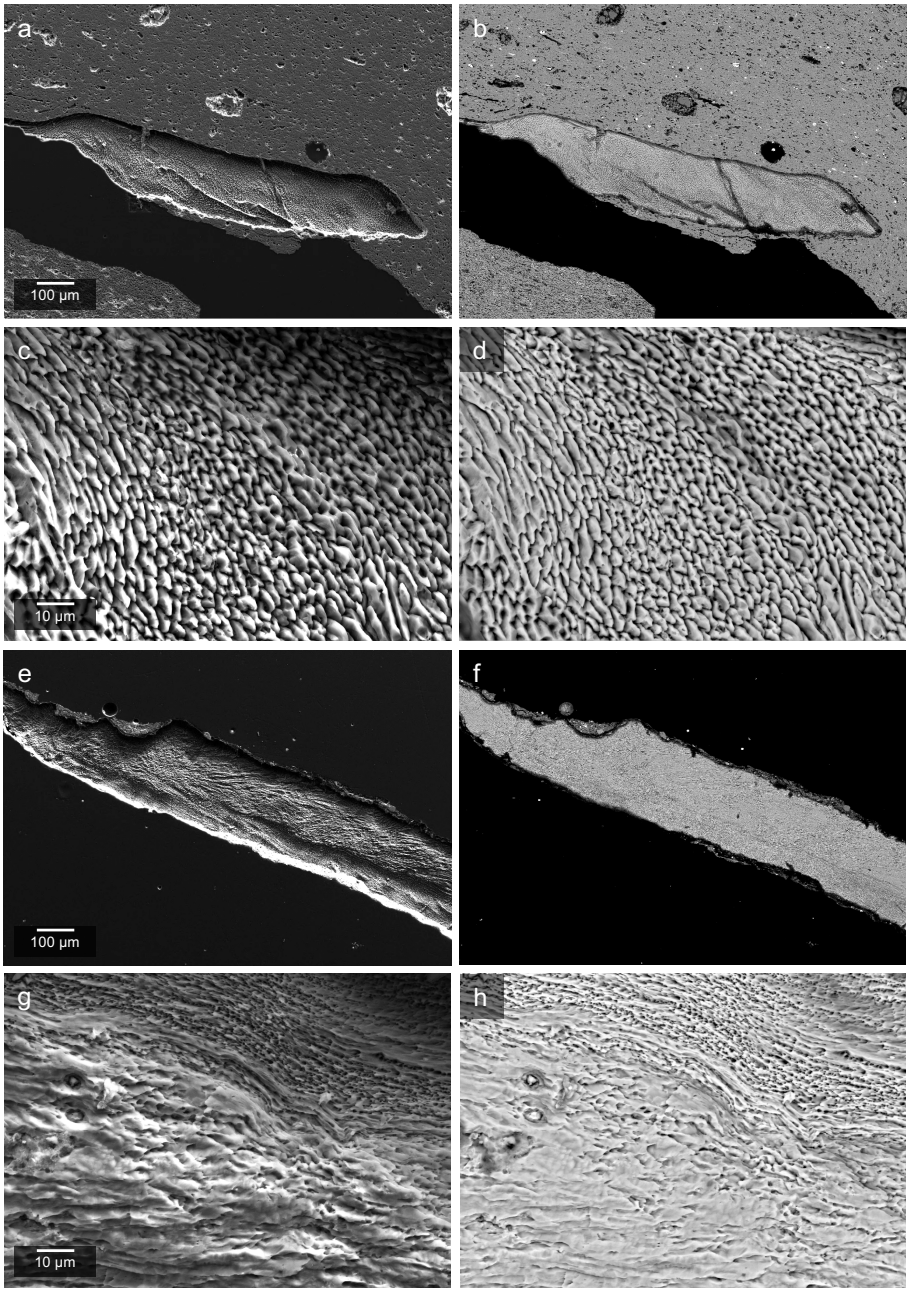

Figure S2.2. Secondary electron (left panels) and backscatter images (right panels) of; a–b) *Paracrurithyris* sp. (Rhynchonellata) specimen from South China (latest Changhsingian, Shangsi); c–d) a capture closing in on the detailed shell structure of the same; e–f) *Teserina* sp. (Strophomenata) from North Italy (earliest Triassic, Tesero); g–h) closer view of the same. Images were taken after weak light acid etching (10 seconds in 5% HCl) of polished gold coated surfaces (required for SIMS measurements).

References

Brand, U. *et al.* The end-Permian mass extinction: A rapid volcanic CO_2 and CH_4-climatic catastrophe. *Chem. Geol.* **323**, 121−144 (2012).

Garbelli, C., Angiolini, L., Shen, S.-Z. Biomineralisation and global change: A new perspective for understanding the end-Permian extinction. *Geology* **45**, 19–22 (2017a).

Garbelli, C. Shell microstructure in Lopingian brachiopods: Implications for fabric evolution and calcification. *Riv. Ital. Paleontol. S.* **123**, 541–560 (2017b).

Garbelli C., Angiolini L., Brand U., Jadoul F. Brachiopod fabric, classes and biogeochemistry: Implications for the reconstruction and interpretation of seawater carbon-isotope curves and records. *Chem. Geol.* **371**, 60–67 (2014).

Ye F., Jurikova H., Angiolini L., Brand U., Crippa G., Henkel D., Laudien J., Hiebenthal C., and Šmajgl D. Variation in brachiopod microstructure and isotope geochemistry under low-pH – ocean acidification conditions. *Biogeosciences* **16**, 617–642 (2019).

S3. Secondary ion mass spectrometry (SIMS) analytical methods

High-spatial resolution *in situ* boron isotope analyses were used to complement data derived from conventional solution-based measurements of dissolved shell powders, as an additional control on preservation and potential influences from embedding matrix contamination (such as clays for example). Previous studies demonstrated SIMS as a reliable approach for measuring $\delta^{11}B$ in marine carbonates, including brachiopods, which is directly comparable to conventional data after correcting for instrumental bias (Jurikova et al., 2019a; Jurikova et al., 2019b). The great advantage of this approach is that we can directly link the isotopic composition of the shell to its structure. This assures that any potential diagenetic alterations of the original shell material, even on a µm-scale level, can be avoided. Moreover, due to its *in situ* nature, SIMS circumvents complex sample preparation steps associated with the solution-based technique, thereby eliminating risks of potential contamination influences to the isotopic values from the surrounding sediment. Ultimately, the high-spatial resolution allows for a measurement of samples too small for the solution-based technique, opening up the possibility to measure specimens with shell thickness of several tens of µm only.

We used the Cameca 1280-HR SIMS instrument at the GFZ German Research Centre for Geosciences – Helmholtz Centre Potsdam to perform *in situ* $\delta^{11}B$ analyses on selected ~30 µm diameter domains within polished brachiopod shells. Our samples were prepared as cm-sized cross-sections of brachiopod shells which were embedded in two epoxy mounts along

with several grains of the calcite Reference Material (RM) IAEA-603; this reference material was subsequently found to be too depleted in boron in order to serve its intended purpose as a drift monitor. Drift monitoring was thus carried by recurring measurement of $\delta^{11}B$ in a selected area of one shell in between the measurement of other samples in the mount. A third mount was also prepared containing the calcite RM UWC-1 to which a $\delta^{11}B_{NBS951}$ value of 7.50 was assigned (Kasemann et al., 2009); the absolute value for the NBS951 boric acid zero-point was set at $^{11}B/^{10}B = 4.04558$ (Palmer & Slack, 1989). Our test portion mass was typically ~5 ng, as determined from crater volume estimates (Fig. S3.1) obtained from white light interferometry in conjunction with an assumed density of $\rho = 2.7$ g cm^{-1} for calcite. This very fine sampling size allowed us to target domains free of visible alteration within the innermost secondary layer of brachiopod shells (Fig. S3.2), which is considered the most suitable shell part for geochemical analyses for its good preservation and lesser sensitivity to vital effects (Rollion-Bard et al., 2019). Prior to analysis all three sample mounts were ultrasonically cleaned in high-purity ethanol for five minutes followed by the deposition of a 35 nm thick high-purity gold coat using an argon sputter coater. Finally, overview images of the entire surface of each sample mount were made using a Nikon Eclipse optical microscope; these images were then loaded in the instrument's point logger software.

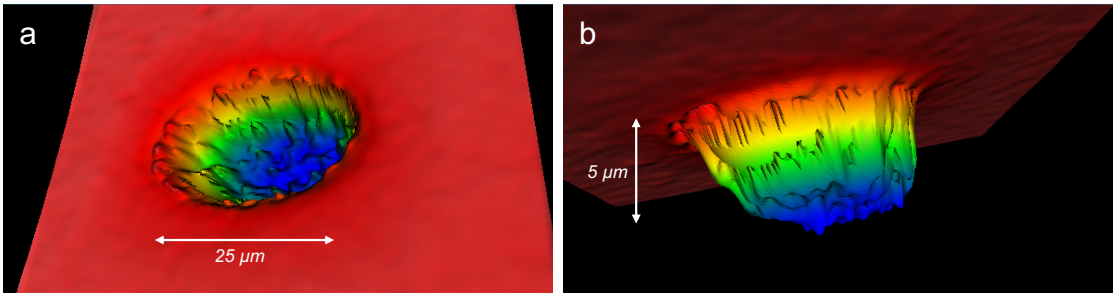

Figure S3.1. 3D model of a typical crater left in a sample or a standard after boron isotope measurements on the SIMS.

We used a $^{16}O^-$ primary beam with a total impact energy of 23 keV operated in Köhler illumination with a primary beam current that varied between ~40 and ~60 nA over the 4 days of our analytical sequence. Prior to initiating data acquisition each spot was pre-sputtered for 100 s using a 35 × 35 µm raster in order to suppress surface contamination and to help establish equilibrium sputtering conditions. Subsequent to the pre-sputtering, automatic beam centering routines were conducted for both X and Y on the instrument's field aperture and for

the X direction on the contrast aperture. Vacuum in our sample chamber ranged from 6.0 to 9.9×10^{-9} over our 4 days of data acquisition.

The secondary side of our SIMS instrument was operated at a mass resolution of $M/\Delta M \approx 2000$, which fully eliminates the $^{10}B^{1}H^{+}$ isobaric interference from the $^{11}B^{+}$ mass station; at this mass resolution the 1280 SIMS instrument is effectively operating at full transmission. A +10 kV extraction potential was applied to our sample to which no offset voltage was applied. A 6000 × 6000 µm square field aperture, equivalent to a ~45 µm field of view, helped to reduce any background which might have resulted from surface contamination near the crater edge.

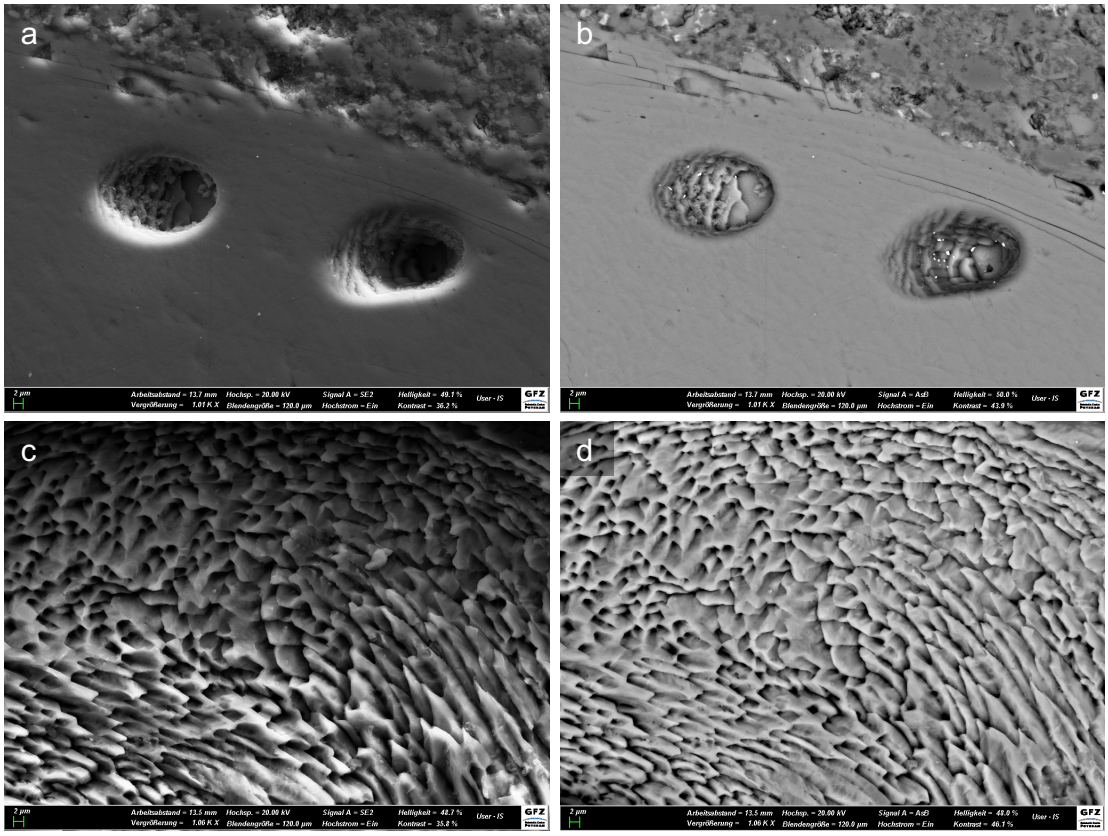

Figure S3.2. An example of SIMS $\delta^{11}B$ analyses in a *Paracrurithyris* sp. specimen (Rhynchonellata) from South China (latest Changhsingian, Shangsi); a) scanning electron microscope (SEM) and, b) backscatter (BSE) images of two craters from measurement within gold coated polished shell surfaces; c) SEM and, d) BSE images after gold removal and light acid etching (10 seconds in 5% HCl) showing excellent preservation of the domains.

Data were collected in multi-collection mode with the secondary magnetic field stabilized with the instrument's NMR field control system. Hamamatsu narrow format electron multipliers located at the L2 and H2 positions were used to detect the $^{10}B^{+}$ and $^{11}B^{+}$ ion

intensities, respectively. Data were collected in 30 integrations each lasting 15 seconds, such that a single analysis including the pre-sputtering and automatic centring routines lasted ~10 minutes. The count rate on the $^{11}B^{+}$ mass station on the UWC-1 RM was typically in the range 5000 to 10000 ions/second, which translated to an uncertainty ~1 to 1.5 ‰ (1s) on the individual analyses. We note that for the samples the count rate was typically much higher (at least double than that on the RM), resulting in a better internal uncertainty. Altogether 82 determinations on the UWC-1 were conducted over the period of 4 days of data acquisition arranged in 8 blocks, resulting in a conservative external repeatability of better than ± 1.4 ‰ (SD; n = 82).

References

Jurikova, H. *et al.* Boron isotope composition of the cold-water coral *Lophelia pertusa* along the Norwegian margin: Zooming into a potential pH-proxy by combining bulk and high-resolution approaches. *Chem. Geol.* **513**, 143–152 (2019a).

Jurikova, H. *et al.* Boron isotope systematics of cultured brachiopods: response to acidification, vital effects and implications for palaeo-pH reconstruction. *Geochim. Cosmochim. Acta* **248**, 370–386 (2019b).

Kasemann, S.A., S.A., Schmidt, D.N., Bijima, J., Foster, G.L. *In situ* boron isotope analyses in marine carbonates and its application for foraminifera and palaeo-pH. *Chem. Geol.* **260**, 138–147 (2009).

Palmer, M.R. & Slack, J.F. Boron isotopic composition of tourmaline from massive sulphide deposits and tourmalinites. *Contrib. Mineral. Petr.* **103**, 434–451 (1989).

Rollion-Bard, C. *et al.* Assessing the biomineralisation processes in the shell layers of modern brachiopods from oxygen isotopic composition and elemental rations: Implications for their use as paleoenvironmental proxies. *Chem Geol.* **524**, 49–66 (2019).

S4. Modelling

S4.1. Model set-up

A geochemical box model was set up to simulate the processes in the global ocean. In the model, the global ocean is represented by 6 boxes: surface water (0–100 m water depth), intermediate water (100–1300 m), and deep water (>1300) for both, Tethys and Panthalassa Oceans (Fig. S4.1). Basin volumes, seafloor areas, and water fluxes were taken from a recent ocean circulation model for the Permian-Triassic boundary (PTB; Winguth et al., 2015). The recently developed REDBIO model (Wallmann et al., 2019) was coupled with the box model to simulate biogeochemical turnover. REDBIO considers the following dissolved tracers: oxygen, nitrate, ammonium, phosphate, ferric iron, ferrous iron, total dissolved sulphide, dissolved inorganic carbon (^{12}C and ^{13}C) and total alkalinity. All tracer inventories change over time due to weathering inputs from land, CO_2 and O_2 fluxes across the ocean–atmosphere interface, nitrogen fixation, denitrification and redox-dependent fluxes at the seabed. Continental weathering and degassing fluxes, surface temperatures and atmospheric pCO_2 were simulated using GEOCARB process formulations (Berner & Kothavala, 2001; Royer et al., 2014), whereas marine $\delta^{13}C$ values were calculated as described in a previous box model (Wallmann et al., 2016).

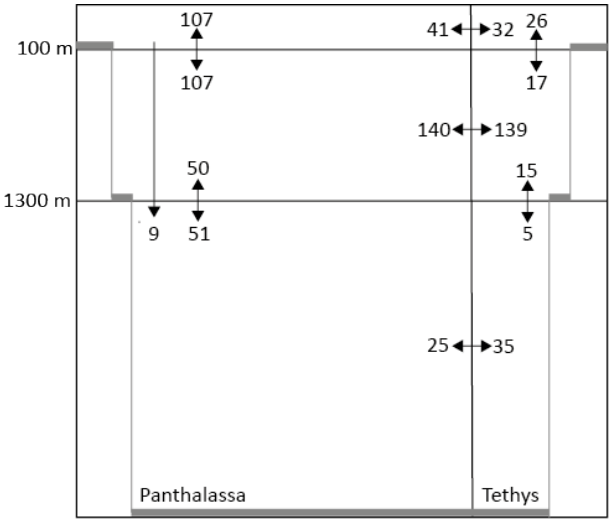

Figure S4.1. Our box model setup. The global ocean is represented by 6 boxes: surface water (0–100 m water depth), intermediate water (100–1300 m), and deep water (>1300) for both, Tethys and Panthalassa. Inventories of the dissolved tracers are allowed to change over time due to weathering inputs from land, CO2 and O2 fluxes across the ocean/atmosphere interface, and redox-dependent fluxes at the seabed (represented by horizontal grey bars). Water fluxes across the box boundaries are given in Sv.

REDBIO was extended to simulate the turnover of stable nitrogen isotopes in the ocean. The model considers total concentrations of dissolved nitrate and ammonium and the

concentrations of ^{15}N-nitrate und ^{15}N-ammonium. ^{15}N fluxes are calculated from the corresponding total N fluxes applying the mole fraction of ^{15}N (Φ^{15}N):

$$^{15}N\text{-}flux = \Phi^{15}N \times N\text{-}flux$$

$$\Phi^{15}N = \frac{^{15}N}{N} = \frac{^{15}N}{^{14}N + ^{15}N}$$

The mole fraction and the commonly used δ^{15}N value (in ‰) are related as:

$$\delta^{15}\mathrm{N} = 1000 \times \left(\frac{\Phi^{15}N}{R_{St} - R_{St} \times \Phi^{15}N} - 1 \right)$$

$$\Phi^{15}\mathrm{N} = \frac{R_{St} \times (1000 + \delta^{15}N)}{1000 + R_{St} \times (1000 + \delta^{15}N)}$$

where air nitrogen that is applied as standard has a ^{15}N/^{14}N ratio of R_{St} = 3676.5 ×10^{-6} (Hoefs, 1997).

The fractionation between ^{15}N and ^{14}N that occurs during the transformation of compound B into A is expressed applying the ^{15}N/^{14}N ratio in these compounds using the fractionation factor α:

$$\alpha_{A-B} = \frac{R_A}{R_B}$$

^{15}N/^{14}N ratios (R) are related to the corresponding ^{15}N mole fraction as:

$$\Phi^{15}\mathrm{N} = \frac{R}{1 + R}$$

$$R = -\frac{\Phi^{15}N}{\Phi^{15}N - 1}$$

Hence, the fractionation factor α can be expressed in terms of mole fractions as:

$$\alpha_{A-B} = \frac{\Phi^{15}N_A \times (\Phi^{15}N_B - 1)}{\Phi^{15}N_B \times (\Phi^{15}N_A - 1)}$$

and the mole fractions that are applied to derive ^{15}N fluxes from N fluxes are calculated as:

$$\Phi^{15}N_A = \frac{\alpha_{A-B} \times \Phi^{15}N_B}{1 + \Phi^{15}N_B \times (\alpha_{A-B} - 1)}$$

Here, we report the fractionation factor in the commonly used δ notation where it takes the form:

$$\epsilon = (1 - \alpha) \times 1000$$

$$\alpha = 1 - \frac{\epsilon}{1000}$$

Applying for example ε = +1.5 ‰ for nitrogen fixation, the diazotroph biomass is 1.5 ‰ depleted in $\delta^{15}N$ relative to the source (atmospheric $\delta^{15}N\text{-}N_2$ = 0 ‰) giving diazotroph biomass a $\delta^{15}N$ signature of −1.5 ‰.

The processes and flux definitions considered in the nitrogen module of the REDBIO model are explained in detail in Wallmann et al. (2019). The corresponding fractionation factors (ε) are listed in Table S4.1. We assume that no $\delta^{15}N$ fractionation takes place during pelagic and benthic PON degradation (Möbius, 2013; Robinson et al., 2012) and that sedimentary $\delta^{15}N$ data document the $\delta^{15}N$ values of planktonic PON formed in the surface ocean. These assumption are also applied in the interpretation of sedimentary $\delta^{15}N$ records covering the PTB (Algeo et al., 2012; Algeo et al., 2007; Cao et al., 2009; Fujisaki et al., 2019; Jia et al., 2012; Knies et al., 2013; Luo et al., 2011; Luo et al., 2014; Saitoh et al., 2014; Schoepfer et al., 2013).

Process	**ε (‰)**	**Source**
N_2-fixation	1.5	*Somes et al., 2013*
Phytoplankton nitrate assimilation	5	*Somes et al., 2013*
Pelagic denitrification	20	*Altabet, 2007*
Benthic denitrification	2	*Somes et al., 2013*
Pelagic PON degradation	0	*Robinson et al., 2012*
Benthic PON degradation, ammonification	0	*Robinson et al., 2012*
Ammonium oxidation to nitrate	3	*Dale et al., 2019*
Anaerobic iron oxidation, nitrate reduced to N_2	20	*this study*
Anaerobic sulfide oxidation, nitrate reduced to N_2	20	*this study*

Table S4.1. Fractionation factors applied in the N isotope model.

S4.2. Standard case scenario

S4.2.1. Model forcing

Volcanic CO_2 degassing was applied as major model forcing since the Permian-Triassic (a 252 Ma) mass extinction (PTME) was very likely triggered by volatile release from Siberian flood basalts. The Siberian flood basalts emplacement started about 300 ka prior to the PTME (Burgess and Bowring, 2015). Close to the negative $\delta^{13}C$ excursion marking the onset of the PTME (Burgess et al., 2014), the emplacement style changed abruptly from dominantly flood lavas to sill intrusions (Burgess et al., 2017). The sill intrusion continued for a period of at least 500 ka into the Triassic (Burgess and Bowring, 2015). The sills intruded the thick

Tunguska basin, composed of evaporite, clastic, carbonate, and hydrocarbon-bearing rocks (Burgess et al., 2017). The negative $\delta^{13}C$ excursion (CIE) is usually ascribed to isotopically depleted carbon released from sedimentary rocks by sill intrusions (Burgess et al., 2017). The metamorphism of sedimentary carbon may have generated up to 120 000 Gt C with $\delta^{13}C$ values of around –25 ‰ to –20 ‰ (Augland et al., 2019; Svensen et al., 2009; Svensen et al., 2018). The degassing of mantle CO_2 from the sills may have released an additional amount of 30 000 Gt C with a $\delta^{13}C$ value of –6 ‰ (Svensen et al., 2018). The total CO_2 flux from Siberian Traps via magma degassing ($\delta^{13}C$ = –6 ‰) has been estimated as 70 000–300 000 Gt CO_2 (Saunders, 2016). The volatile content of the mantle plume feeding the flood basalt was probably enriched in ^{13}C by the assimilation of metasomatized lithospheric material, which may have further enhanced the degassing flux (Broadley et al., 2018). Volcanic activity and degassing at convergent continental margins induced by the closure of the Tethys Ocean may have contributed to the degassing in the aftermath of the extinction as documented by the correlation between multiple ash layers and negative carbon excursions in Tethys sediments (Shen et al., 2012; Wang et al., 2019). The CO_2 degassing curve applied in the standard model run is consistent with these observations (Fig. S4.2). The total degassing flux applied over the model period (–500 to 500 ka relative to the negative carbon isotope excursion, CIE) amounts to 386 760 Gt CO_2. The maximum annual emission rate applied in the model (2.55 Gt CO_2 yr^{1}) is much smaller than the current anthropogenic rate (about 38 Gt CO_2 yr^{-1} from fossil fuels in 2018; Crippa et al., 2019) whereas the overall emission over the peak period (113 000 Gt CO_2 at 0–45 ka relative to CIE) exceeds estimates for the total anthropogenic CO_2 emission in the 20^{th}–21^{th} century (up to 5 000 Gt CO_2).

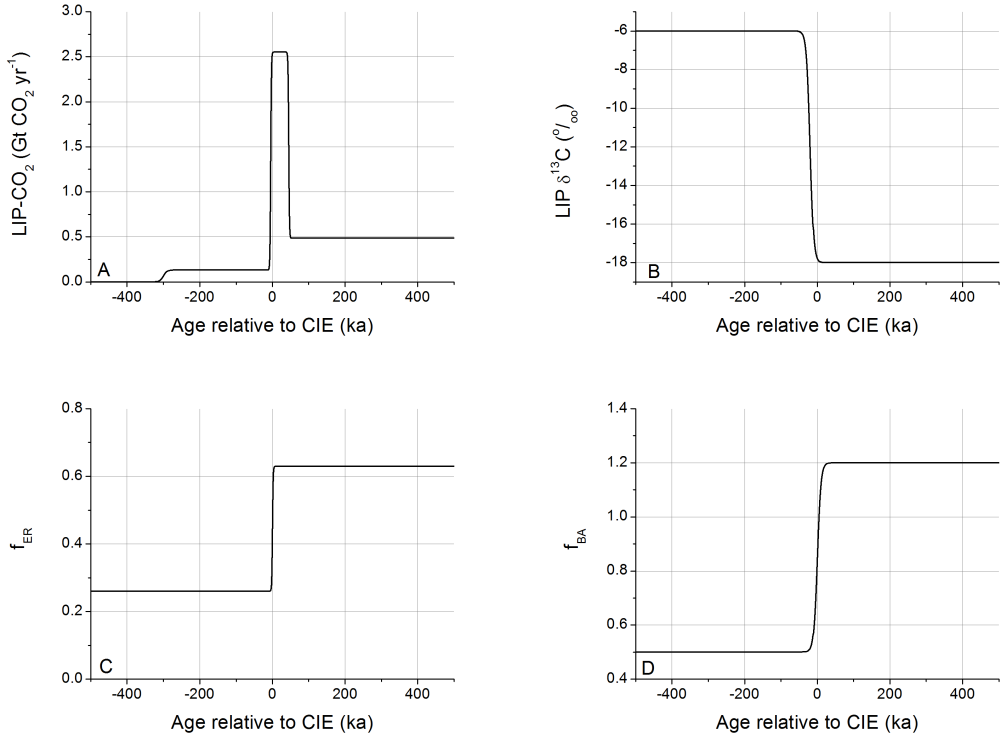

Figure S4.2. Model forcing. Time (age) is defined in ka relative to the negative carbon isotope excursion (CIE). a) CO_2 flux induced by Siberian flood basalts and sill intrusions; b) isotopic composition of CO_2 released by flood lavas and sill intrusions; c) continental erosion rate (f_{ER}) normalized to modern value (Hay et al., 2006); and d) basalt weathering flux (f_{BA}) of exposed areas normalized to modern value (Mills et al., 2014).

Rates of physical erosion increased drastically over the PTB as indicated by a strong rise in terrigenous sedimentation at the seafloor (Algeo and Twitchett, 2010; Hay et al., 2006). Since erosion affects silicate and organic carbon weathering and riverine inputs of particulate phosphorus and iron, the increase in global erosion rate was considered as additional model forcing (Fig. S4.2). Moreover, we consider that rates of basalt weathering were enhanced by the emplacement of Siberian flood basalts (Fig. S4.2; Mills et al., 2014).

S4.2.2. Model results

Global carbon cycling and climate were strongly affected by the model forcing (Figs. S4.3). The partial pressure of CO_2 in the atmosphere (pCO_2) was lowest over the Late Permian, reached a peak at 44 ka after the CIE and remained at an enhanced level over the Early Triassic. The calculated pCO_2 values are broadly consistent with proxy-based estimates over the model period (Godderis et al., 2008; McElwain et al., 2009; Retallack, 2001; Witkowski et al., 2018). Resulting changes in global mean surface temperature (T_{atm}) and sea surface

temperature (SST) are also consistent with previous model- and proxy-based estimates (Joachimski et al., 2012; Schobben et al., 2014; Sun et al., 2012; Winguth et al., 2015). Rates of continental silicate, carbonate and particulate organic carbon (POC) weathering increased due to the rise in pCO_2, T_{atm}, erosion rate and basalt exposure over the PTB. Most of the CO_2 emitted by the LIP was rapidly consumed and converted into bicarbonate by silicate and carbonate weathering. Marine export production rose in response to the increase in SST and nutrient input. The increase in export production and depletion of dissolved oxygen in the ocean led to a fourfold increase in organic carbon burial across the PTB as previously derived from sediment records (Algeo et al., 2013). Carbonate burial declined at the PTB due to the strong acidification of surface waters and increased after the PTB in response to the enhanced alkalinity level in seawater caused by chemical weathering. Changes in carbonate burial calculated by the model are consistent with those derived from stable Ca and Sr isotope records across the PTB (Silva-Tamayo et al., 2018; Vollstaedt et al., 2014).

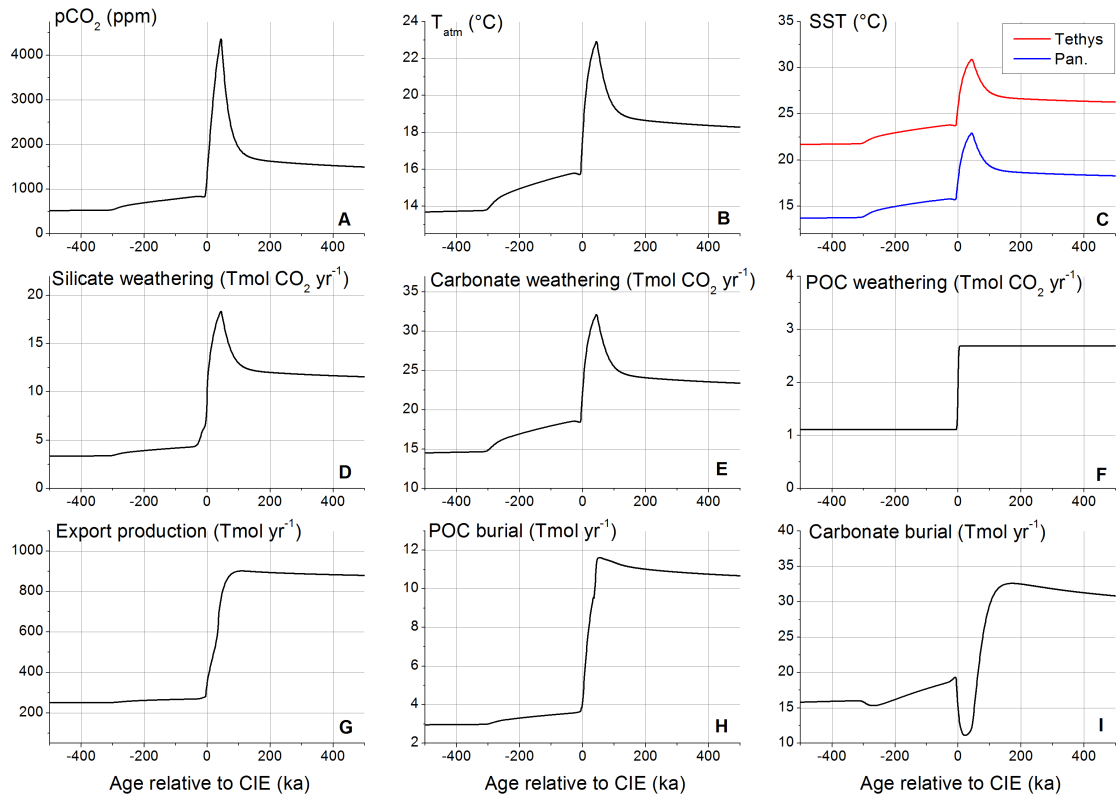

Figure S4.3. Carbon cycling and climate change during the standard model run. a) Partial pressure of CO_2 in the atmosphere; b) global mean surface temperature; c) sea surface temperature in Tethys and Panthalassa; d) global rate of silicate weathering (granite + basalt weathering); e) global rate of carbonate weathering; f) global rate of organic carbon weathering; g) export production of organic carbon in the global ocean across 100 m water depth; h) burial of particulate organic carbon (POC) in sediments at the global seafloor; and i) burial of neritic carbonate on the global shelf.

Concentrations of dissolved inorganic carbon and total alkalinity increased over the PTB and remained on a very elevated level over the Early Triassic due to enhanced weathering (Fig. S4.4). Since calcifying phytoplankton emerged late over the Mesozoic, pelagic carbonates were not yet present and carbonate burial occurred only on the shelf. Under these conditions, carbonate compensation is less efficient than in the modern ocean such that surface waters were strongly oversaturated with respect to calcite (Zeebe and Westbroek, 2003). The calcite saturation state was calculated as $[Ca^{2+}] \times [CO_3^{2-}]/K_{sp}$ where $[Ca^{2+}]$ is the dissolved calcium concentration, $[CO_3^{2-}]$ the concentration of dissolved carbonate anions and K_{sp} the solubility product of calcite (Zeebe and Wolf-Gladrow, 2001). The Ca concentration was set to a constant value of 12 mM representative for Late Permian seawater (Farkaš et al., 2007) whereas $[CO_3^{2-}]$ was calculated as a dynamic model variable. The pH and $\delta^{13}C$ values calculated in the standard run are consistent with observations shown in Figure 2 (in the manuscript). The standard case was in fact constructed by varying the CO_2 release from the Siberian LIP (Fig. S4.2) within the given constraints until the model was able to reproduce the pH and $\delta^{13}C$ records (Fig. S4.4).

The $\delta^{13}C$ composition of neritic carbonate deposited on the Tethys shelf was taken from Cao et al. (2009), Shen et al. (2013), Jiang et al. (2015), Galfetti et al. (2017), Saitoh et al. (2014), Sun et al. (2019) on the Yangtze platform (South China), from Korte & Kozur (2005) and Magaritz & Holser (1991) in Southern Alps, from Shen et al. (2013) and Zhang et al. (2018) on the southern shelf of Palaeotethys, from Shen et al. (2013) on the northern and Richoz (2006) on the southern shelf of Neotethys. The $\delta^{13}C$ values for carbonate and organic sediments for Panthalassa were taken from Musashi et al. (2001) in shallow-water carbonates in the central part of the ocean, Takahashi et al. (2010) in the deep, and Fenton et al. (2007), Wignall et al. (1998), Grasby & Beuchamp (2008), Algeo et al. (2012), Grasby et al. (2016), Grasby et al. (2019) and Schoepfer et al. (2012) in the high latitudes.

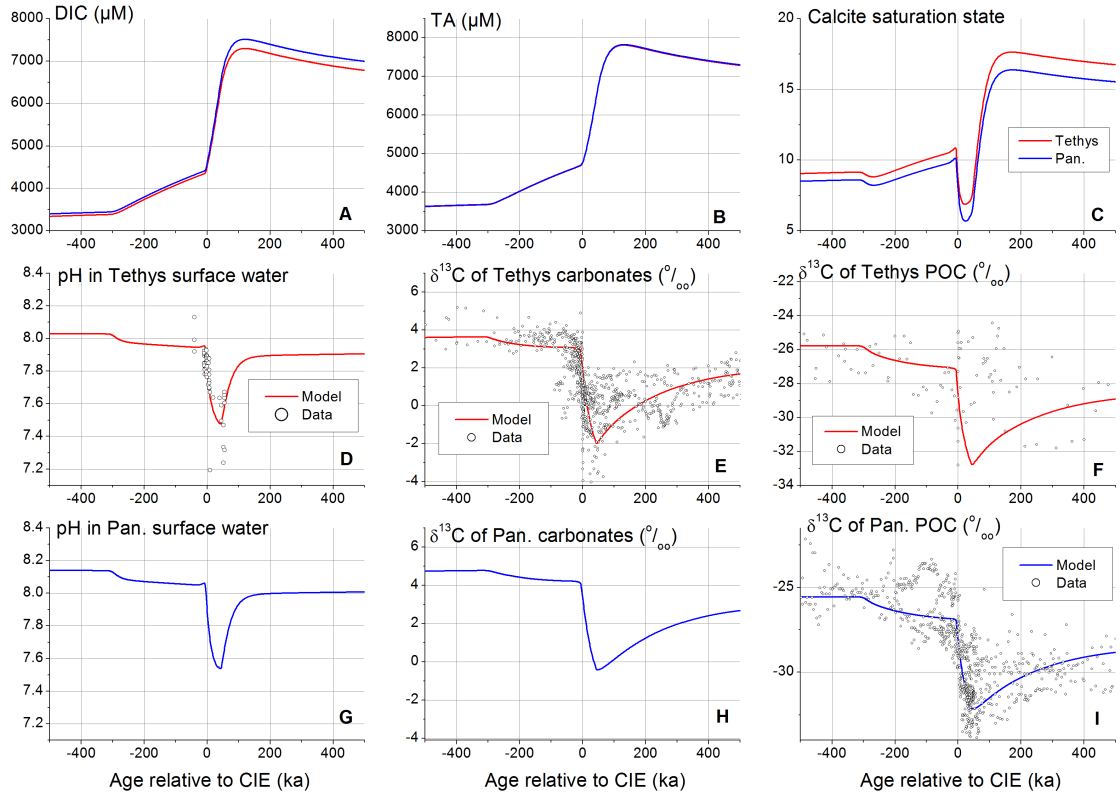

Figure S4.4. Marine carbonate system and carbon isotopes during the standard model run. a) dissolved inorganic carbon (DIC) in surface water (0 – 100 m water depth) of Tethys and Panthalassa; b) total alkalinity (TA) in surface water (0 – 100 m water depth) of Tethys and Panthalassa. Tethys results are barely visible because the Panthalassa results plot on top of the Tethys results; c) saturation state of surface water (0 – 100 m water depth) with respect to calcite in Tethys and Panthalassa; d) pH in Tethys surface water, data are derived from boron isotope values as described in the main text; e) $\delta^{13}C$ values of neritic carbonate deposited on the Tethys shelf, data sources are given in text. f) $\delta^{13}C$ values of organic carbon in sediments deposited on the Tethys seafloor, data are taken from (Cao et al., 2009; Saitoh et al., 2014; Sun et al., 2019); g) pH in Panthalassa surface water; h) $\delta^{13}C$ values of neritic carbonate deposited on the shelf; i) $\delta^{13}C$ values of organic carbon in sediments deposited on the Panthalassa seafloor, data sources are given in text.

Dissolved oxygen concentrations in sub-surface waters strongly declined soon after the PTB and remained at low values over the Early Triassic due to the increase in export production and respiration (Fig. S4.5). Oxygen concentrations in the surface ocean were maintained at a high level by the exchange with the atmosphere. Models indicate that the oxygen content of the Late Permian atmosphere (23–24.5 vol-%) was substantially higher than in the modern atmosphere (Bergman et al., 2004; Royer et al., 2014). Hence, we applied a constant atmospheric partial pressure of 0.237 atm in our model to simulate the oxygen exchange between the surface ocean and the atmosphere. Oxygen was completely consumed in Tethys intermediate water 50 ka after the onset of the CIE. In all other ocean boxes, low but significant oxygen concentrations were maintained with minimum values of 10 μM in Tethys

deep water, 4 µM in Panthalassa intermediate water and 18 µM in the deep Panthalassa. Dissolved nitrate increased at the CIE because nitrogen fixation was promoted by the rise in SSTs caused by LIP degassing. Nitrate declined again after pelagic and benthic denitrification kicked in due to the spread of low-oxygen conditions. Dissolved sulphide accumulated in Tethys intermediate water when oxygen and nitrate were depleted. In all other ocean boxes, sulphide accumulation was inhibited by the presence of dissolved oxygen and nitrate.

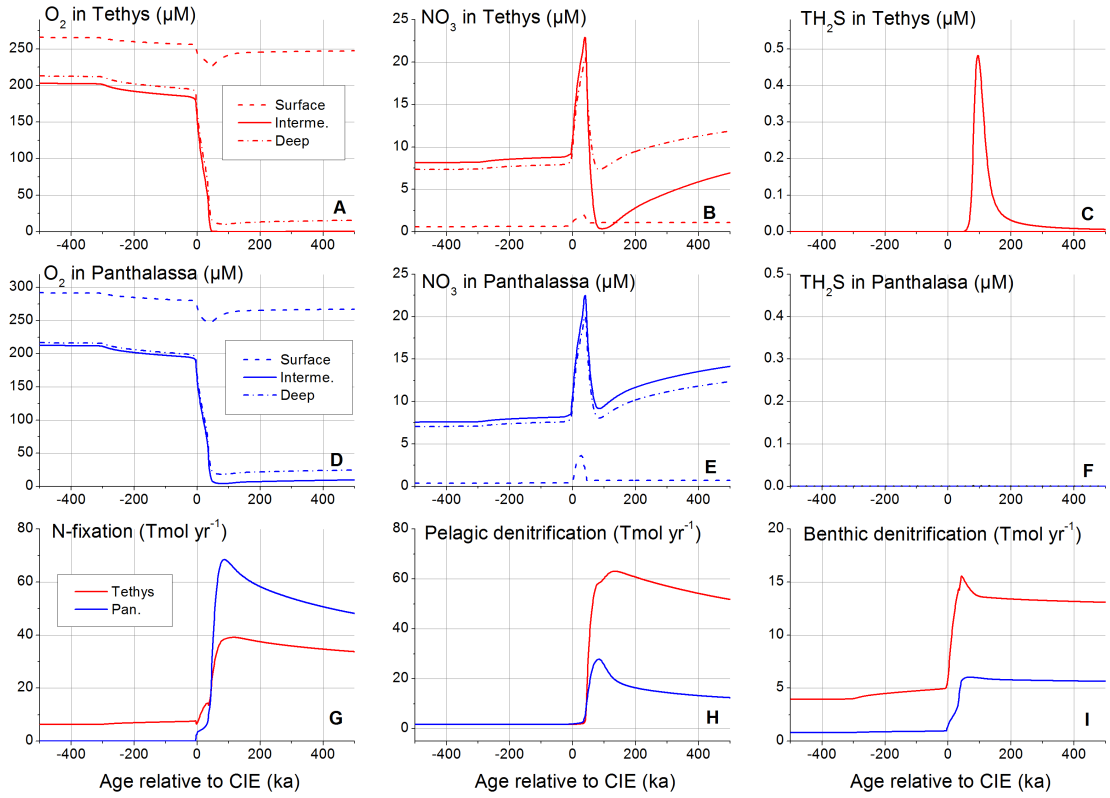

Figure S4.5. Redox state of the ocean in the standard model run. a) Dissolved oxygen in Tethys surface water (0–100 m), intermediate water (100–1300 m) and deep water (>1300 m); b) dissolved nitrate in Tethys surface water (0 – 100 m), intermediate water (100–1300 m) and deep water (>1300 m); c) dissolved sulphide in Tethys surface water (0–100 m), intermediate water (100–1300 m) and deep water (>1300 m); d) dissolved oxygen in Panthalassa surface water (0–100 m), intermediate water (100–1300 m) and deep water (>1300 m); e) dissolved nitrate in Panthalassa surface water (0–100 m), intermediate water (100–1300 m) and deep water (>1300 m); f) dissolved sulphide in Panthalassa surface water (0–100 m), intermediate water (100–1300 m) and deep water (>1300 m); g) Nitrogen fixation in Tethys and Panthalassa surface water; h) pelagic denitrification in Tethys and Panthalassa sub-surface water (>100 m); i) Benthic denitrification in Tethys and Panthalassa sediments.

The global sub-surface ocean attained a low-oxygen state after the PTB where oxygen and nitrate rather than sulphate were used as terminal electron acceptor for organic matter degradation. This redox state is characteristic for modern oxygen minimum zones (Canfield,

2006). It also promotes uranium accumulation in marine sediments (Anderson et al., 2019). Hence, the redox state predicted by the model is consistent with uranium isotope and Th/U records indicating wide-spread uranium uptake in sediments after the PTB (Elrick et al., 2017; Zhang et al., 2018).

Dissolved ammonium, phosphate and iron were release from sediments under low-oxygen conditions after the PTB and supported the rise in export production and respiration in a positive feedback loop (Fig. S4.6).

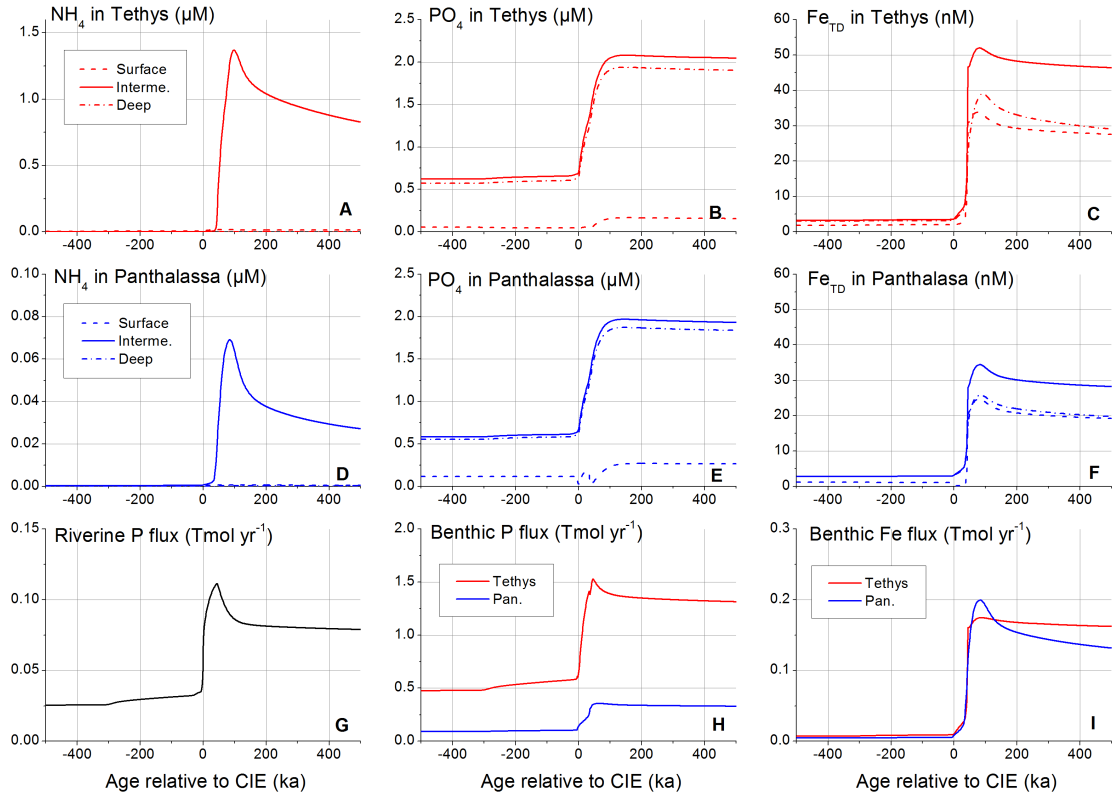

Figure S4.6. Dissolved nutrient concentrations in the standard model run. a) Dissolved ammonium in Tethys surface water (0–100 m), intermediate water (100–1300 m) and deep water (>1300 m); b) dissolved phosphate in Tethys surface water (0–100 m), intermediate water (100–1300 m) and deep water (>1300 m); c) dissolved iron (Fe^{2+} + Fe^{3+}) in Tethys surface water (0–100 m), intermediate water (100–1300 m) and deep water (>1300 m); d) dissolved ammonium in Panthalassa surface water (0–100 m), intermediate water (100–1300 m) and deep water (>1300 m); e) dissolved phosphate in Panthalassa surface water (0–100 m), intermediate water (100–1300 m) and deep water (>1300 m); f) dissolved iron (Fe^{2+} + Fe^{3+}) in Panthalassa surface water (0–100 m), intermediate water (100–1300 m) and deep water (>1300 m); g) riverine flux of dissolved P into the global ocean; h) benthic release of dissolved phosphate from Tethys and Panthalassa sediments; and i) benthic release of dissolved iron (Fe^{2+}) from Tethys and Panthalassa sediments.

Due to the strong denitrification under low oxygen conditions (Fig. S4.5), plankton growth is largely limited by nitrate, while nitrogen-fixation is limited by phosphate. Upon the consumption of oxygen in the ocean, nitrate is the most favourable electron acceptor, which is respired and subsequently lost from the system in the form of N_2. Loss of nitrogen leaves the inorganic nutrients relatively enriched in phosphate, which is thought to benefit N_2-fixing diazotrophs (see e.g. Bristow et al., 2017 for more details). Thus, deviations in the nitrate to phosphate ratio may be used to assess the importance of denitrification and nitrogen fixation in the ocean. The modelled plankton growth and changes in the limiting nutrients are also highly consistent with restructuration of marine plankton communities observed in the geological record (Shen et al., 2015). The increase in nitrogen-fixation and productivity after the PTB was triggered by the rise in SSTs (Fig. S4.3). Nitrogen-fixation was further supported by the increase in the riverine phosphate flux (Fig. S4.6) induced by enhanced surface temperatures (Fig. S4.3) and physical erosion rates (Fig. S4.2). Dissolved ammonium accumulated in the anoxic intermediate water of the Tethys Ocean but was oxidized by dissolved oxygen in all other ocean boxes. Our model results are consistent with geological observations indicating high rates of nitrogen fixation in the Early Triassic (Xie et al., 2010) but do not support the hypothesis that ammonium reached toxic levels in the global ocean contribution to the mass extinction (Sun et al., 2019).

The isotopic composition of sedimentary nitrogen ($\delta^{15}N$) calculated in the model largely reflects the composition of marine organic matter formed in the surface ocean (Fig. S4.7). We note that, in this case, the model fit is not as good as for the other parameters presented, principally due to less data available and greater variability between the records. There are, however, notable differences in the $\delta^{15}N$ records between Tethys and Panthalassa and from Late Permian to Early Triassic that can be resolved by the model. The Permian values in Tethys are generally more depleted than those in Panthalassa. This difference is related to the temperature-dependence of nitrogen fixation (NF). NF is suppressed by the low SST calculated for the Panthalassa Ocean (Fig. S4.3) while the higher SST values in the Tethys Ocean support NF (Fig. S4.5). Since NF leads to the uptake of isotopically depleted N_2 from the atmosphere, the suppression of this process in the Panthalassa Ocean causes a marked $\delta^{15}N$ contrast between the two ocean basins that is also documented in the sedimentary record (Fig. S4.7). $\delta^{15}N$ values decline in both basins at the CIE due to the rapid rise in NF (Figs. S4.5 and S4.7). Subsequently, $\delta^{15}N$ values increase due to pelagic denitrification that is consuming a large portion of the dissolved nitrate pool in sub-surface waters and

preferentially removes the light isotope. After the excess nitrate produced by the rise in NF at the CIE is consumed, the $\delta^{15}N$ values decline due to the ongoing NF. The Early Triassic $\delta^{15}N$ values are lower than those over the Late Permian due to the higher level of NF over the Triassic, a difference that is also observed in sedimentary records (Fig. S4.7).

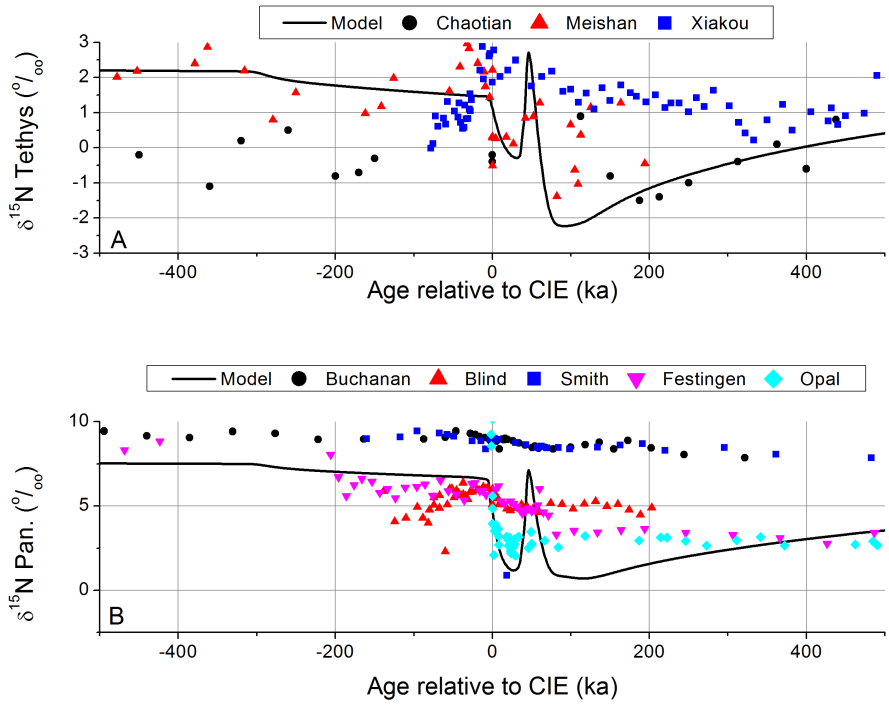

Figure S4.7. $\delta^{15}N$ values of sediments deposited in a) Tethys, and b) Panthalassa ocean. Model results for the standard case are compared to previously published sediment data (Algeo et al., 2012; Algeo et al., 2007; Cao et al., 2009; Fujisaki et al., 2019; Grasby and Beauchamp, 2009; Grasby et al., 2016; Jia et al., 2012; Knies et al., 2013; Luo et al., 2011; Luo et al., 2014; Saitoh et al., 2014; Schoepfer et al., 2013; Sun et al., 2019).

S4.3. Model sensitivity tests

S4.3.1. Ocean redox conditions

The redox conditions in the model ocean largely depend on nutrient availability. Unfortunately, major nutrient fluxes such as the rate of nitrogen fixation, the removal rate of dissolved iron via scavenging and the riverine P flux into the ocean are largely unconstrained even for the modern ocean (Dale et al., 2015; Gruber, 2016; Wallmann, 2010). Hence, it is possible to create a completely anoxic or oxic model ocean by varying the nutrient fluxes into the ocean. As an example, we run simulations with enhanced and reduced riverine P fluxes (Fig. S4.8).

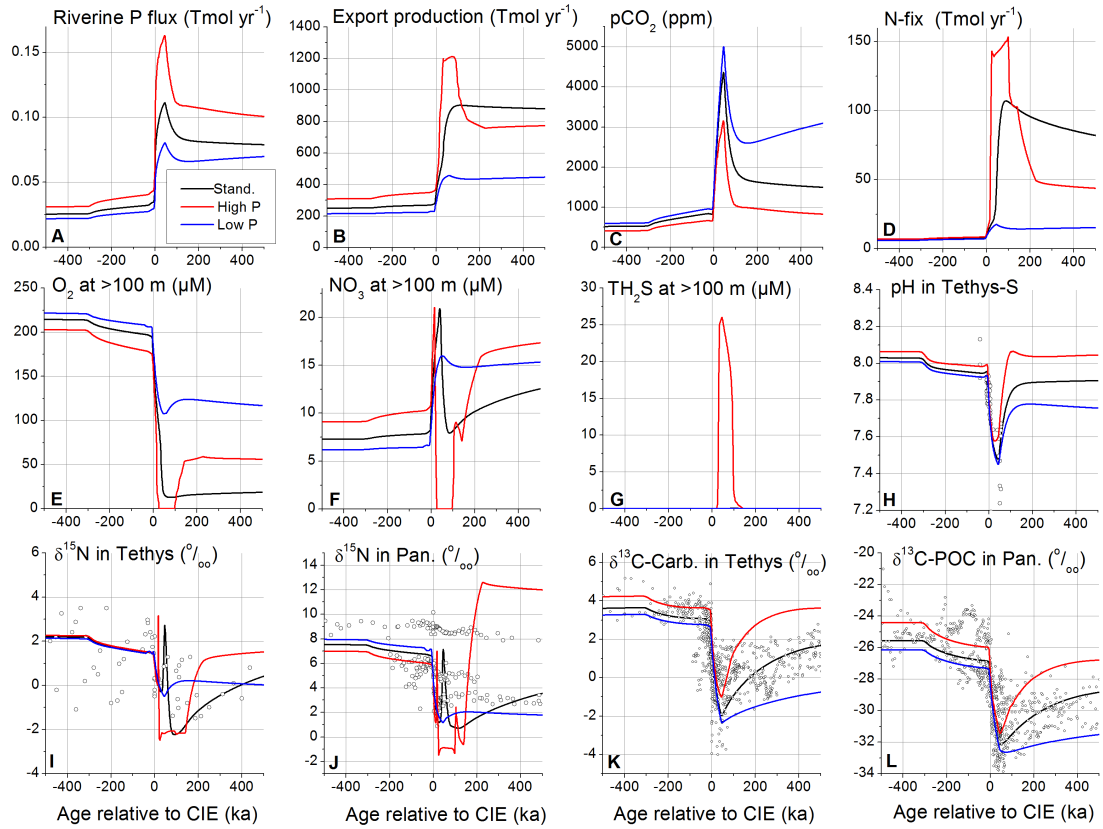

Figure S4.8. Results of the standard case as well as model runs with high and low riverine P fluxes. a) Riverine P flux. b) Global export production. c) Atmospheric partial pressure of CO_2. d) Global rate of N fixation. e) Global mean oxygen concentration at >100 m water depth. f) Global mean nitrate concentration at >100 m. g) Global mean sulphide concentration at >100 m. h) pH in Tethys surface water. i) $\delta^{15}N$ in Tethys sediments. j) $\delta^{15}N$ in Panthalassa sediments. k) $\delta^{13}C$ in Tethys shelf carbonate. l) $\delta^{13}C$ in organic carbon accumulating at the Panthalassa seafloor.

A 50 % increase of the riverine P flux leads to a strong increase in export production and nitrogen fixation and a corresponding drawdown of atmospheric pCO_2. The productivity decreases after the degassing maximum due to the decrease in atmospheric CO_2 and the corresponding decline in SSTs. The entire sub-surface ocean turns anoxic at 25–100 ka after the CIE and dissolved sulphide accumulates in both ocean basins at >100 m water depth. Subsequently, modelled oxygen and nitrate values recover due to the decline in pCO_2. However, the fit to the proxy data is affected by the P increase. Modelled $\delta^{13}C$ values rise to a post-CIE level that is significantly higher than suggested by the data because more organic carbon is buried in marine sediments. The pH minimum is not as distinct as recorded by the boron isotope data due to the diminished pCO_2 peak. Modelled $\delta^{15}N$ values are strongly diminished during the anoxic period since the entire dissolved nitrate pool at >100 m water depth is lost by denitrification such that the marine isotope signal reflects the negative value

induced by nitrogen fixation. During the subsequent period, $\delta^{15}N$ values reach a level that is much higher than recorded in sediments because nitrogen fixation is diminished by the pCO_2 drawdown causing a corresponding decline in SSTs. The misfit to the proxy data suggests that the LIP degassing did not induce anoxia in the global subsurface ocean. However, the global decline in sub-surface oxygen calculated for the standard run may promote anoxia/euxinia in up-welling regions and oxygen minimum zones that are not resolved by the box model due to its conceptual setup.

Export production and nitrogen fixation are strongly diminished when the riverine P flux is reduced by about 50 %. Atmospheric pCO_2 values increase since less CO_2 is taken up by the biological carbon pump. The entire ocean is well oxygenated due to the decline in respiration. Modelled $\delta^{13}C$ values remain at a post-CIE level that is significantly lower than suggested by the data because less organic carbon is buried in marine sediments. The $\delta^{15}N$ values calculated for the Tethys do not show the strong decrease after the CIE that is observed in the data because nitrogen fixation remains at a low level over the entire model period. The misfit between modelled and observed $\delta^{13}C$ and $\delta^{15}N$ values indicates that the ocean was not fully oxygenated after the PTB. This conclusion is strongly supported by previously published proxy records for the PTB and the Early Triassic indicating wide-spread anoxic or low-oxygen conditions (Bond and Wignall, 2010; Elrick et al., 2017; Schobben et al., 2015; Zhang et al., 2018).

The standard model run and the sensitivity tests suggest that the deep ocean remained in a low-oxygen state and that most of the deep-sea ecosystem was probably not seriously affected by sulphide poisoning. Sulphide formation and poisoning may have contributed to the marine mass extinction at the continental margins of the Tethys Ocean and in up-welling regions of the Panthalassa Ocean where low-oxygen and high nutrient concentrations in ascending sub-surface waters may have promoted anoxic/euxinic conditions.

S4.3.2 Seawater pH

In the standard case, an empirical brachiopod calibration curve was used to calculate pH values from boron isotope data (Lécuyer et al., 2002). In the following simulation, we use the borate ion calibration curve as an alternative approach to convert boron isotope data to seawater pH (Klochko et al., 2006) and test whether the model is able to reproduce the

resulting pH values. The inorganic borate ion calibration yields pH values that are significantly lower than those derived from the brachiopod calibration (Fig. S4.9). Seawater pH is related to the carbonate ion concentration that is in turn largely controlled by the efficiency of neritic carbonate burial. Hence, we increased the kinetic constant for carbonate burial to lower the carbonate ion concentration, decrease seawater pH, and reproduce the borate-calibrated pH values.

In the model, burial of neritic carbonate (BCN) is calculated as:

$$BCN = k_{BCN} (\Omega - 1) BCN_H$$

where BCN_H is the Holocene rate of neritic carbonate burial (10 Tmol yr^{-1}; Kleypas, 1997) and Ω is the calcite saturation state which is a dynamic model variable (Fig. S4.4). In the standard case, we chose a value of 0.2 yr^{-1} for the kinetic constant k_{BCN}. The Holocene surface ocean is strongly oversaturated with respect to calcite with tropical Ω values of about 6 (Kleypas et al., 2001) such that k_{BCN} = 0.2 yr^{-1} yields the modern burial rate. With this approach, we assume that Permian/Triassic carbonate compensation via neritic carbonate burial is as efficient as in the modern ocean. In the sensitivity test, we increased the kinetic constant to k_{BCN} = 0.3 yr^{-1} to lower the seawater pH values and fit the borate-calibrated pH values (Fig. S4.9).

The rate of neritic carbonate burial increases when the kinetic constant for burial is enhanced (Fig. S4.9). Concentrations of dissolved inorganic carbon and alkalinity decline due to the increase in carbonate burial. The saturation state is strongly diminished because burial is now more efficient than in the standard case.

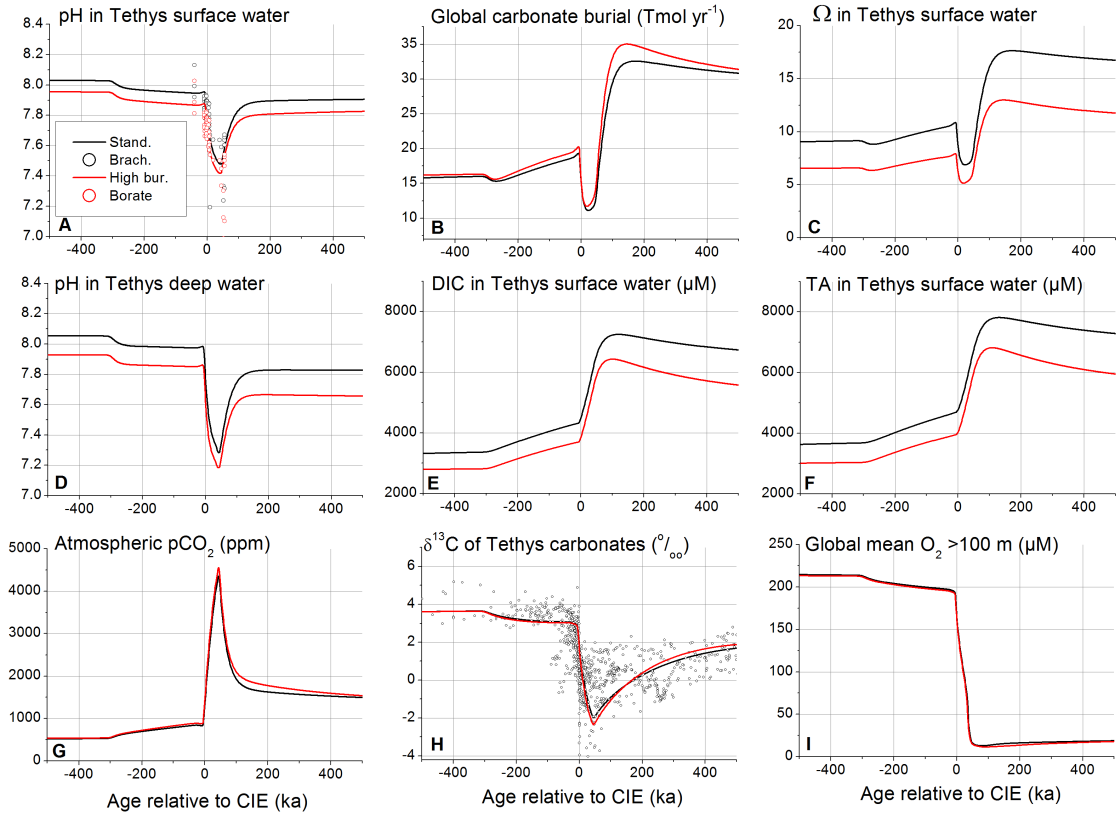

Figure S4.9. Results of the standard case (black lines, k_{BCN} = 0.2 yr^{-1}) and a model run with enhanced carbonate burial (red lines, k_{BCN} = 0.3 yr^{-1}). a) Seawater pH in Tethys surface water, symbols indicate pH values derived from boron isotope data using brachiopod calibration (black), and inorganic borate ion relationship (red). b) Burial rate of neritic carbonate on the global shelf. c) Saturation state of Tethys surface water with respect to calcite. d) Seawater pH in Tethys deep water (>1300 m water depth). e) Dissolved inorganic carbon in Tethys surface water. f) Total alkalinity in Tethys surface water. g) Atmospheric partial pressure of CO_2. h) $\delta^{13}C$ of carbonates deposited on the Tethys shelf. i) Global mean oxygen concentration at >100 m water depth.

Atmospheric pCO_2 is slightly enhanced because carbonate burial produces CO_2 that is released into the atmosphere. The oxidation state of the sub-surface ocean and isotopic composition of shelf carbonates are not significantly affected by the enhanced carbonate burial because these variables are largely controlled by the nutrient budget of the ocean that was not significantly affected by the k_{BCN} change. The simulation shows that it is possible to reproduce the pH values derived from the borate calibration without affecting model results other than those related to the carbonate system. However, in this simulation we had to assume that the efficiency of neritic carbonate burial was enhanced over the Late Permian and Early Triassic with respect to the modern ocean. Following the doctrine of uniformity, we prefer the concept applied in the standard case and, hence, the pH values derived from the brachiopod calibration. Additional model runs were conducted to reproduce the sharp pH

minimum at 10 ka after the CIE (results not shown). However, these simulations showed that it is not possible to reproduce such a strong and sharp pH decline to pH <7.4 without violating the constraints given by LIP degassing and $\delta^{13}C$ records. Considering that sub-surface waters may attain pH values <7.4 (Fig. S4.9), we propose that the very low pH values indicated by the boron isotope data for 10 ka after the CIE may reflect local up-welling episodes where brachiopods calcified in acidic water masses ascending from the sub-surface.

Overall, the data and the modelling suggest that global and simultaneous ocean acidification, warming and deoxygenation may have contributed to the global marine mass extinction whereas sulphide poisoning may have been a regional rather than global process largely limited to the continental margins of the Tethys Ocean and up-welling regions in the Panthalassa Ocean.

References

Winguth, A.M.E., Shields, C.A. & Winguth, C. Transition into a Hothouse World at the Permian-Triassic boundary-A model study. *Palaeogeogr. Palaeoclimatol. Palaeoecol.* **440**, 316−327 (2015).

Wallmann, K. *et al.* Periodic changes in the Cretaceous ocean and climate caused by marine redox see-saw. *Nat. Geosci.* **12**, 456–462 (2019).

Berner, R.A. & Kothavala, Z. GEOCARB III: A revised model of atmospheric CO_2 over Phanerozoic time. *Am. J. Sci.* **301**, 182−204 (2001).

Royer, D.L., Donnadieu, Y., Park, J., Kowalczyk, J. & Godderis, Y. Error analysis of CO_2 and O_2 estimates from the long-term geochemical model GEOCARBSULF. *Am. J. Sci.* **314**, 1259−1283 (2014).

Wallmann, K., Schneider, B. & Sarnthein, M. Effects of eustatic sea-level change, ocean dynamics, and nutrient utilization on atmospheric pCO_2 and seawater composition over the last 130,000 years. *Clim. Past.* **12**, 339–375 (2016).

Hoefs, J. Stable Isotope Geochemistry. Springer-Verlag, Berlin (1997).

Möbius, J. Isotope fractionation during nitrogen remineralization (ammonification): Implications for nitrogen isotope biogeochemistry. *Geochim. Cosmochim. Acta* **105**, 422−432 (2013).

Robinson, R. S. *et al*. A review of nitrogen isotopic alteration in marine sediments. *Paleoceanography* **27**, 13 (2012).

Algeo, T. *et al.* Evidence for a diachronous Late Permian marine crisis from the Canadian Arctic region. *Geol. Soc. Am. Bull.* **124**, 1424−1448 (2012).

Algeo, T. J. *et al.* Sequencing events across the Permian-Triassic boundary, Guryul Ravine (Kashmir, India). *Palaeogeogr. Palaeoclimatol. Palaeoecol*. **252**, 328−346 (2007).

Cao, C. Q. *et al.* Biogeochemical evidence for euxinic oceans and ecological disturbance presaging the end-Permian mass extinction event. *Earth Planet. Sci. Lett.* **281**, 188−201 (2009).

Fujisaki, W. *et al.* Redox condition and nitrogen cycle in the Permian deep mid-ocean: A possible contrast between Panthalassa and Tethys, *Glob. Planet. Change* **172**, 179−199 (2019).

Jia, C. *et al.* Microbial response to limited nutrients in shallow water immediately after the end-Permian mass extinction. *Geobiology* **10**, 60−71 (2012)

Knies, J., Grasby, S. E., Beauchamp, B. & Schubert, C. J. Water mass denitrification during the latest Permian extinction in the Sverdrup Basin, Arctic Canada. *Geology* **41**, 167−170 (2013).

Luo, G. M. Enhanced nitrogen fixation in the immediate aftermath of the latest Permian marine mass extinction. *Geology* **39**, 647−650 (2011).

Luo, G. M., Xie, S. C., Liu, D. & Algeo, T. J. Microbial influences on paleoenvironmental changes during the Permian-Triassic boundary crisis. *Sci. China Earth Sci.* **57**, 965−975 (2014).

Saitoh, M. *et al.* Nitrogen isotope chemostratigraphy across the Permian-Triassic boundary at Chaotian, Sichuan, South China. *J. Asian Earth Sci.* **93**, 113−128 (2014).

Schoepfer, S. D. *et al.* Termination of a continent-margin upwelling system at the Permian-Triassic boundary (Opal Creek, Alberta, Canada). *Glob Planet. Change* **105**, 21−35 (2013).

Somes, C. J., Oschlies, A. & Schmittner, A. Isotopic constraints on the pre-industrial oceanic nitrogen budget. *Biogeosciences* **10**, 5889−5910 (2013).

Altabet, M. A. Constraints on oceanic N balance/imbalance from sedimentary ^{15}N records. Biogeosciences **4**, 75−86 (2007).

Dale, A. W., Bourbonnais, A., Altabet, M., Wallmann, K. & Sommer, S. Isotopic fingerprints of benthic nitrogen cycling in the Peruvian oxygen minimum zone. *Geochim Cosmochim Acta* 245, 406−425 (2019).

Burgess, S. D. & Bowring, S. A. High-precision geochronology confirms voluminous magmatism before, during, and after Earth's most severe extinction. *Sci. Adv.* **1**, 14 (2015).

Burgess, S. D., Bowring, S. & Shen, S. Z. High-precision timeline for Earth's most severe extinction. *Proc. Natl. Acad. Sci. U. S. A.* **111**, 3316−3321 (2014).

Burgess, S. D., Muirhead, J. D. & Bowring, S. A. Initial pulse of Siberian Traps sills as the trigger of the end-Permian mass extinction. *Nat. Comm.* **8**, 6 (2017).

Augland, L. E. *et al.* The main pulse of the Siberian Traps expanded in size and composition. *Sci. Rep.* **9**, 12 (2019).

Svensen, H. *et al.* Siberian gas venting and the end-Permian environmental crisis. *Earth Planet. Sci. Lett.* **277**, 490−500 (2009).

Svensen, H. H. *et al.* Sills and gas generation in the Siberian Traps. *Philos. Trans. R. Soc. A* **376**, 18 (2018).

Saunders, A. D. Two LIPs and two Earth-system crises: the impact of the North Atlantic Igneous Province and the Siberian Traps on the Earth-surface carbon cycle. *Geol. Mag*. **153**, 201−222 (2016).

Broadley, M. W., Barry, P. H., Ballentine, C. J., Taylor, L. A. & Burgess, R. End-Permian extinction amplified by plume-induced release of recycled lithospheric volatiles. *Nat. Geosci.* **11**, 682–687 (2018).

Shen, J., *et al.* Negative C-isotope excursions at the Permian-Triassic boundary linked to volcanism. *Geology* **40**, 963−966 (2012).

Wang, X. D. *et al.* Convergent continental margin volcanic source for ash beds at the Permian-Triassic boundary, South China: Constraints from trace elements and Hf-isotopes. *Palaeogeogr. Palaeoclimatol. Palaeoecol.* **519**, 154−165 (2019).

Crippa, M. *et al.* Fossil CO_2 and GHG emissions of all world countries. 2019 Report, European Union, Luxembourg (2019)

Algeo, T. J. & Twitchett, R. J. Anomalous Early Triassic sediment fluxes due to elevated weathering rates and their biological consequences. *Geology* **38**, 1023−1026 (2010).

Hay, W. W. *et al.* Evaporites and the salinity of the ocean during the Phanerozoic: Implications for climate, ocean circulation and life. *Palaeogeogr. Palaeoclimatol. Palaeoecol* **240**, 3−46 (2006).

Mills, B., Daines, S. J., & Lenton, T. M. Changing tectonic controls on the long-term carbon cycle from Mesozoic to present. *Geochem. Geophys. Geosyst.* **15**, 4866−4884 (2014).

Godderis, Y. *et al.* Causal or casual link between the rise of nannoplankton calcification and a tectonically-driven massive decrease in Late Triassic atmospheric CO_2? *Earth Planet. Sci. Lett.* **267**, 247−255 (2008).

McElwain, J. C., Wagner, P. J. & Hesselbo, S. P. Fossil Plant Relative Abundances Indicate Sudden Loss of Late Triassic Biodiversity in East Greenland. *Science* **324**, 1554−1556, 2009.

Retallack, G. J. A 300-million-year record of atmospheric carbon dioxide from fossil plant cuticles. *Nature* **411**, 287−290 (2001).

Witkowski, C. R., Weijers, J. W. H., Blais, B., Schouten, S. & Damste, J. S. S. Molecular fossils from phytoplankton reveal secular P_{CO2} trend over the Phanerozoic. *Sci. Adv.* **4**, 7 (2018).

Joachimski, M. M. *et al.* Climate warming in the latest Permian and the Permian-Triassic mass extinction. *Geology* **40**, 195−198 (2012).

Schobben, M., Joachimski, M. M., Korn, D., Leda, L. & Korte, C. Palaeotethys seawater temperature rise and an intensified hydrological cycle following the end-Permian mass extinction. *Gondwana Res.* **26**, 675−683 (2014).

Sun, Y. D., *et al.* Lethally Hot Temperatures During the Early Triassic Greenhouse. *Science* **338**, 366−370 (2012).

Algeo, T. J. *et al.* Plankton and productivity during the Permian-Triassic boundary crisis: An analysis of organic carbon fluxes. *Global Planet. Change* **105**, 52−67 (2013).

Silva-Tamayo, J. C. *et al.* Global perturbation of the marine calcium cycle during the Permian-Triassic transition. *Geol. Soc. Am. Bull.* **130**, 1323−1338 (2018).

Vollstaedt, H. *et al.* The Phanerozoic $d^{88/86}Sr$ record of seawater: New constraints on past changes in oceanic carbonate fluxes. *Geochim. Cosmochim. Acta* **128** (2014).

Zeebe, R. & Westbroek, P. A simple model for the $CaCO_3$ saturation state of the ocean: The "Strangelove", the "Neritan", and the "Cretan" Ocean. *Geochem. Geophy. Geosy.* **4**, 1104 (2003).

Zeebe, R. & Wolf-Gladrow, D. CO_2 in Seawater: Equilibrium, Kinetics and Isotopes. Elsevier, Amsterdam (2001).

Farkaš, J. *et al.* Calcium isotope budget of Phanerozoic oceans: Implications for chemical evolution of seawater and its causative mechanism. *Geochim. Cosmochim. Acta* **71**, 5117−5134 (2007).

Shen, S.-Z. *et al*. High-resolution $\delta^{13}C_{carb}$ chemostratigraphy from latest Guadalupian through earliest Triassic in South China and Iran. *Earth Planet. Sci. Lett*. **375**, 156–165 (2013).

Jiang, H., Joachimski, M.M., Wignall, P.B., Zhang, M., Lai, X. A delayed end-Permian extinction in the deep-water locations and its relationship to temperature trends (Bianyang, Guizhou Province, South China) *Palaeogeogr. Palaeoclimatol. Palaeoecol.* **440**, 690–695 (2015).

Galfetti, T. *et al.* Timing of Early Triassic carbon cycle perturbations inferred from new U-Pb ages and ammonoid biochronozones. *Earth Planet. Sci. Lett*. **258**, 593–604 (2017).

Korte, C. & Kozur, H.W. Carbon isotope stratigraphy across the Permian/Triassic boundary at Jolfa (NW-Iran), Peitlerkofel (Sas de Pütia, Sass de Putia), Pufels (Bula, Bulla), Tesero (all three Southern Alps, Italy) and Gerennavár (Bükk Mts., Hungary). *J. Alpine Geol.* **47**, 119–135 (2005).

Magaritz, M. & Holser, W.T. The Permian-Triassic of the Gartnerkofel-1 Core (Carnic Alps, Austria): Carbon and Oxygen Isotope Variations. *Abh. Geol. B.-A.* **45**, 149–163 (1991).

Zhang, F. *et al.* Multiple episodes of extensive marine anoxia linked to global warming and continental weathering following the latest Permian mass extinction. *Sci. Adv.* **4**, e1602921 (2018).

Richoz, S. Stratigraphy and Carbon Isotope Study of the Upper Permian and Lower Triassic in some localities of the Neotethyan realm (Turkey, Oman, Iran). *Mémoires de Géologie (Lausanne) no*. **46** (2006).

Musashi, M., Isozaki Y., Koike, T. & Kreulen R. Stable carbon isotope signature in mid-Panthalassa shallow-water cabonates across the Permo-Triassic boundary: evidence for ^{13}C-depleted superocean. *Earth Planet. Sci. Lett.* **191**, 9−20 (2001).

Takahashi, S., Kaiho K., Oba M. & Kakegawa, T. A smooth negative shift of organic carbon isotope ratios at an end-Permian mass extinction horizon in central pelagic Panthalassa. *Earth Planet. Sci. Lett.* **292**, 532−539 (2010).

Fenton, S. *et al.* Changes in biomarker abundances and sulfur isotopes of pyrite across the Permian-Triassic (P/Tr) Schuchert Dal section (East Greenland). *Earth Planet. Sci. Lett.* **262**, 230−239 (2007).

Wignall, P.B., Morante, R. & Newton, R. The Permo-Triassic transition in Spitsbergen: $\delta^{13}C_{org}$ chemostratigraphy, Fe and S geochemistry, facies, fauna and trace fossils. *Geol. Mag.* **135**, 47−62 (1998).

Grasby, S.G. & Beuchamp, B. Intrabasin variability of the carbon-isotope record across the Permian-Triassic transition, Sverdrup Basin, Arctic Canada. *Chem. Geol.* **253**, 141−150 (2008).

Grasby, S.E., Beauchamp, B. & Knies, J. Early Triassic productivity crises delayed recovery from world's worst mass extinction. *Geology* **44**, 779−782 (2016).

Grasby, S.E., Knies, J., Beauchamp, B., Bond, D.P.G., Wignall, P. & Sun, Y. Global warming leads to Early Triassic nutrient stress across northern Pangea. *Geol. Soc. Am. Bull.* (2019)

Schoepfer, S.D., Henderson,C.M., Garrison, G.H. & Ward, P.D. Cessation of a productive coastal upwelling system in the Panthalassic Ocean at the Permian-Triassic Boundary. *Palaeogeogr. Palaeoclimatol. Palaeoecol.* **331–314**, 181–188 (2012).

Bergman, N. M., Lenton, T. M. & Watson, A. J. COPSE: A new model of biogeochemical cycling over Phanerozoic time. *Am J. Sci.* **304**, 397−437 (2004).

Royer, D. L., Donnadieu, Y., Park, J., Kowalczyk, J. & Godderis, Y. Error analysis of CO_2 and O_2 estimates from the long-term geochemical model GEOCARBSULF. *Am J. Sci.* **314**, 1259−1283 (2014).

Canfield, D. E. Models of oxic respiration, denitrification and sulfate reduction in zones of coastal upwelling. *Geochim. Cosmochim. Acta* **70**, 5753−5765 (2006).

Anderson, R. F. *et al.* Deep-Sea Oxygen Depletion and Ocean Carbon Sequestration During the Last Ice Age. *Glob. Biogeochem. Cy.* **33**, 301−317 (2019).

Elrick, M., *et al.* Global-ocean redox variation during the middle-late Permian through Early Triassic based on uranium isotope and Th/U trends of marine carbonates. *Geology* **45**, 163−166 (2017).

Zhang, F. F., Algeo, T. J., Romaniello, S. J., Cui, Y., Zhao, L. S., Chen, Z. Q., and Anbar, A. D.: Congruent Permian-Triassic delta U-238 records at Panthalassic and Tethyan sites: Confirmation of global-oceanic anoxia and validation of the U-isotope paleoredox proxy. *Geology* **46**, 327−330 (2018).

Bristow, L.A., Mohr, W., Ahmerkamp, S. & Kuypers, M.M. Nutrients that limit growth in the ocean. *Curr. Biol.* **27**, R431−R510 (2017).

Shen, J. *et al.* Marine productivity changes during the end-Permian crisis and Early Triassic recovery. *Earth-Sci. Rev.* **149**, 136–162 (2015).

Xie, S. C. *et al.* Cyanobacterial blooms tied to volcanism during the 5 m.y. Permo-Triassic biotic crisis. *Geology* **38**, 447−450 (2010).

Sun, Y. D. *et al.* Ammonium ocean following the end-Permian mass extinction. *Earth Planet Sci. Lett.* **518**, 211−222 (2019).

Grasby, S. E. and Beauchamp, B.: Latest Permian to Early Triassic basin-to-shelf anoxia in the Sverdrup Basin, Arctic Canada. *Chemical Geology* **264**, 232−246 (2009).

Grasby, S. E., Beauchamp, B., and Knies, J.: Early Triassic productivity crises delayed recovery from world's worst mass extinction. *Geology* **44**, 779−782 (2016).

Dale, A. W. *et al.* A revised global estimate of dissolved iron fluxes from marine sediments. *Glob. Biogeochem. Cy.* **29**, 691−707 (2015).

Gruber, N. Elusive marine nitrogen fixation. *Proc. Natl. Acad. Sci. U.S.A*. **113**, 4246−4248 (2016).

Wallmann, K. Phosphorus imbalance in the global ocean? *Global Biogeochem. Cy.* **24**, GB4030 (2010).

Bond, D. P. G. & Wignall, P. B. Pyrite framboid study of marine Permian-Triassic boundary sections: A complex anoxic event and its relationship to contemporaneous mass extinction. *Geol. Soc. Am. Bull.* **122**, 1265−1279 (2010).

Schobben, M. *et al.* Flourishing ocean drives the end-Permian marine mass extinction, Proc. Natl. Acad. Sci. U.S.A. **112**, 10298−10303 (2015).

Klochko, K., Kaufman, A.J., Yao, W.S., Byrne, R.H. & Tossell, J.A. Experimental measurement of boron isotope fractionation in seawater. *Earth Planet. Sci. Lett.* **248**, 267 –285 (2006).

Kleypas, J. A. Modeled estimates of global reef habitat and carbonate production since the Last Glacial Maximum. *Paleoceanography* **12**, 533−545 (1997).

Kleypas, J. A., Buddemeier, R. W. & Gattuso, J. P. The future of coral reefs in an age of global change. *Int J Earth Sci* **90**, 426−437 (2001).

S5. Comparison with atmospheric pCO_2 estimates from stomatal indices

A comparison of our reconstructed atmospheric pCO_2 values (standard case model scenario based on the measured $\delta^{11}B$ values) to those previously derived from stomatal indices modified by Cui & Kump (2015) and based on Retallack (2013) is shown in Figure S5.1. The comparison between the two records is not straightforward largely due to the different temporal resolutions and age models used. However, the overall relative pCO_2 trends compare reasonably well, with low pre-event values in Late Permian, a sharp prominent peak in pCO_2 close to the boundary, followed by a partial drawdown of CO_2 in Early Triassic, but with overall higher background values than in the Late Permian. The increase in atmospheric pCO_2 values derived from stomatal indices precedes by about 1 Ma our sharp CO_2 peak (Fig. S5.1a). This could be potentially explained by the recent developments in dating of the PTB and revised geochronology of the extinction (Burgess et al., 2014) that is accounted for in our work and age model, but not in the earlier studies, and/or further revision of stratigraphic correlations over the past years. A tentative comparison of both records is also presented where the age scales were adjusted to fit the relative pCO_2 trends (Fig. S5.1b). Note that for the purpose of this comparison the x-axis of our record was expanded, while the x-axis of the stomatal record was compressed relative to Figure S5.1a (hence the latter now also shows stomatal data from Cui & Kump, 2015 and Rettalack, 2013 not shown in panel a). Ultimately,

it is also worth noting that these pCO_2 records are based on data from two completely different and independent approaches, underscoring the potential for future cross-calibrations of the two methods.

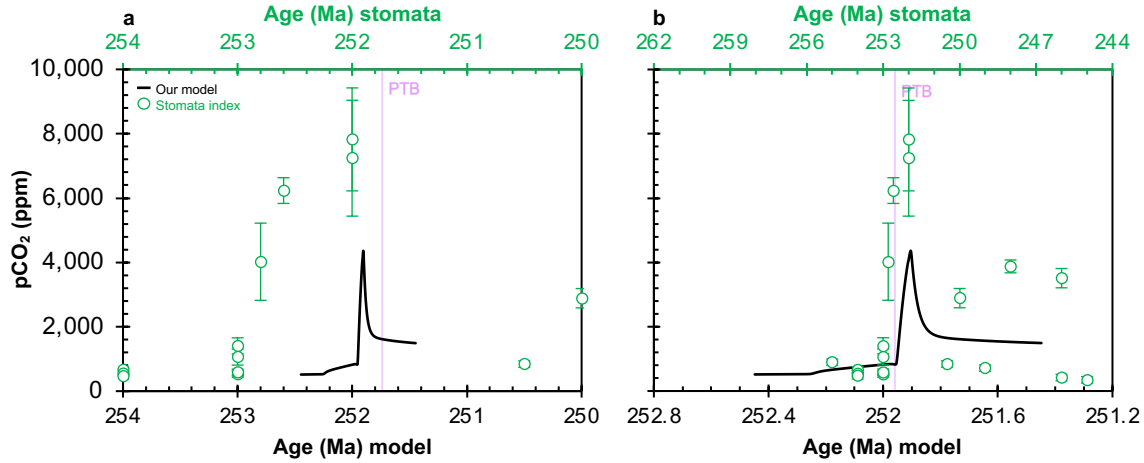

Figure S5.1 Changes in atmospheric pCO_2 over the Permian-Triassic boundary (PTB) as constrained by our standard case model scenario, compared to data from stomatal indices from Cui & Kump (2015) based on Retallack (2013); a) both records plotted next to each other; b) age scales of both records adjusted to match relative pCO_2 trends (note the different upper and lower x-axes, also when compared to panel a).

References

Cui, Y. & Kump, L.R. Global warming and the end-Permian extinction event: Proxy and modeling perspectives. *Earth-Sci. Rev.* **149**, 5–22 (2015).

Retallack G.J. Permian and Triassic greenhouse crises. *Gondwana Res.* **24**, 90–103 (2013). 2

Burgess, S.D., Bowring, S. & Shen, S.-Z. High-precision timeline for Earth's most severe extinction. *Proc. Natl. Acad. Sci. U.S.A.* **111**, 3316–3321 (2014).